On the impact of an offshore bathymetric anomaly on surf zone rip channels

B. Castelle,[1] V. Marieu,[1] G. Coco,[2] P. Bonneton,[1] N. Bruneau,[3] and B. G. Ruessink[4]

Received 4 July 2011; revised 6 February 2012; accepted 10 February 2012; published 31 March 2012.

[1] We use a nonlinear morphodynamic model to demonstrate that the presence of a single persistent offshore bathymetric anomaly strongly affects the formation, nonlinear evolution and saturation of surf zone rip channels. In the case of an offshore bump or trough and waves with oblique incidence, a rip channel shoreward of the anomaly is enforced by the more seaward alongshore variability in depth. The degree of rip channel enforcement is controlled by the strength of the rotational nature of surf zone rip current circulations, which is, in turn, driven by differential broken wave energy dissipation induced by wave refraction across the offshore bathymetric anomaly. The alongshore location of this forced rip channel is more stable with increasing offshore anomaly amplitude, decreasing offshore wave obliquity and decreasing bathymetric anomaly distance to the shore. Simulations show that rip channel behavior downdrift and updrift of the offshore perturbation are different. In our numerical experiments, downdrift rip channels have systematically larger alongshore scales, smaller alongshore migration rates and more erosive megacusps than those updrift. Rip channels therefore self-organize into patterns of different alongshore scales and migration rates as a result of an alongshore perturbation in the wave forcing enforced by wave refraction across an offshore bathymetric anomaly. These simulations are qualitatively corroborated by video observations of sandbar behavior during a down-state sequence at a site with a persistent offshore trough.

Citation: Castelle, B., V. Marieu, G. Coco, P. Bonneton, N. Bruneau, and B. G. Ruessink (2012), On the impact of an offshore bathymetric anomaly on surf zone rip channels, *J. Geophys. Res.*, *117*, F01038, doi:10.1029/2011JF002141.

1. Introduction

[2] Rip channels along wave-dominated beaches are ubiquitous and striking patterns in the sand. They typically consist of both longshore-oriented feeder channels and an offshore-directed rip neck channel that extends throughout the surf zone and incises shallow shore-connected or non-connected shoals [*Brander and Cowell*, 2003]. A rip head bar is also commonly observed seaward in a relatively shore-normal orientation aligned with the rip neck [*Brander and Short*, 2000]. Rip channels prevail as a rhythmic or quasi-rhythmic pattern with an alongshore wavelength of typically several times the surf zone width, i.e., O(100 m). Breaking waves on rip channel morphology force strong jet-like offshore-directed currents called rip currents [*MacMahan et al.*, 2006]. The resulting surf zone circulations are both a key element of mixing in the nearshore and a major hazard to beachgoers [*Scott et al.*, 2009; *Dalrymple et al.*, 2011].

[3] Self-organization models based on linear stability analysis [e.g., *Deigaard et al.*, 1999; *Falqués et al.*, 2000; *Calvete et al.*, 2005; *Klein and Schuttelaars*, 2006] or nonlinear solution of the shallow water equations coupled to sediment transport [e.g., *Reniers et al.*, 2004; *Garnier et al.*, 2006; *Drønen and Deigaard*, 2007; *Smit et al.*, 2008; *Castelle and Ruessink*, 2011] have established that rip channels and other three-dimensional (3-D) sandbar patterns, such as crescentic sandbars, form through the positive feedback between flow (waves and currents), sediment processes and the evolving seabed morphology without requiring a template (edge wave) in the hydrodynamics [*Coco and Murray*, 2007]. Nonlinear morphodynamic models allow examination of temporal changes in the wavelength and the amplitude of the 3-D patterns resulting from merging and splitting of rip channels that are typically observed in the field [*Van Enckevort et al.*, 2004]. So far, all the existing nonlinear analysis studies assumed alongshore-uniform initial beach geometry and wave forcing, with three notable exceptions. First, *Reniers et al.* [2004] used an alongshore nonuniform wavefield by including directional spreading in the initial wave conditions. They showed that the directional spreading affects the behavior of rip channels. Second, *Castelle et al.* [2010a, 2010b] addressed the impact of a crescentic outer bar on inner bar rip channel formation. This

[1]UMR EPOC 5805, CNRS, Université de Bordeaux, Avenue des Facultés, Talence, France.
[2]Environmental Hydraulic Institute, IH Cantabria, Universidad de Cantabria, Santander, Spain.
[3]National Laboratory of Civil Engineering, Estuaries and Coastal Zones Division, Lisbon, Portugal.
[4]Institute for Marine and Atmospheric Research, Department of Physical Geography, Faculty of Geosciences, Utrecht University, Utrecht, Netherlands.

0148-0227/12/2011JF002141

numerical study showed that alongshore variability in outer bar depth, and the relative importance of wave breaking versus wave focusing by refraction across the outer bar, is crucial to the inner bar rip channel development. For well-developed outer bar crescentic patterns, inner bar rip channels ultimately couple to the outer alongshore length scales, corroborating existing observations [e.g., *Ruessink et al.*, 2007; *Price and Ruessink*, 2011]. Third, *Tiessen et al.* [2011] addressed the influence of preexisting rhythmic surf zone bed forms on the subsequent nonlinear evolution of rip channels. They showed that the final dominant rip spacing was most of the time different than that obtained by running the numerical model with the same conditions over an initial alongshore-uniform bathymetry.

[4] Recent observations indicate that morphological features seaward of a surf zone strongly control shoreline variability [*Bender and Dean*, 2003; *McNinch*, 2004; *Schupp et al.*, 2006] and surf zone wave-driven circulations [e.g., *Shepard and Inman*, 1950; *Long and Özkan-Haller*, 2005; *Dalrymple et al.*, 2011]. Most of the studies addressing existing perturbation-shoreline coupling are essentially descriptive [e.g., *McNinch*, 2004; *Browder and McNinch*, 2006; *Schupp et al.*, 2006], with no insight in the underlying physics. Notable exceptions are the theoretical works addressing the development of shoreline instabilities induced by very oblique waves [e.g., *Falqués et al.*, 2011] and potentially low-angle wave incidence [*Idier et al.*, 2011], that are essentially based on the coupling between the surf and shoaling zones. *Bender and Dean* [2003, 2005] investigated wave transformation caused by the processes of wave refraction, diffraction and reflection across an offshore bathymetric anomaly to address the formation of a salient, but they did not compute sediment transport and resulting morphological evolution. Some authors [e.g., *Shepard and Inman*, 1950; *Long and Özkan-Haller*, 2005] examined rip current dynamics for specific beach configurations but did not explore the morphological evolution of rip channels. Overall, nonlinear morphodynamic numerical models have not been used to explore the sensitivity of rip channel behavior to an offshore bathymetric anomaly (i.e., seabed perturbation). This is addressed in this contribution.

[5] In section 2 we present the nonlinear morphodynamic model that describes morphological developments of 3-D surf zone patterns. We present the model by introducing the governing equations and corresponding assumptions, along with an introduction of the methods used to identify the linear/nonlinear/saturation regimes of the rip channels, to quantify rip spacing and alongshore migration rates, and to address the degree of enforcement of initial rip current circulations through wave refraction across the offshore bathymetric anomaly. Results are presented in section 3. We describe in detail a reference case simulation, showing that rip channel behavior downdrift and updrift of the offshore bathymetric anomaly are different. We further qualitatively address the influence of the offshore perturbation characteristics and wave angle on surf zone rip channel evolution. Then, differences in rip spacing and migration rates are quantified at the start of the saturation regime. A discussion is presented in section 4. We link downdrift rip channel behavior with the strength of surf zone rip current circulations enforced by wave refraction across the offshore bathymetric anomaly. Our proof of concept is then qualitatively compared with video observations of sandbar behavior during a down-state sequence at a site with a persistent offshore perturbation; and, furthermore, we discuss the limitations of our model. Finally, conclusions are provided in section 5.

2. Method

2.1. Nonlinear Morphodynamic Model

[6] The nonlinear morphodynamic model used herein couples a spectral wave model, a time- and depth-averaged flow model, an energetic-type sediment transport model, and the bed level continuity equation to compute bed level changes. This model contains the essential physics to describe the formation, nonlinear evolution and the saturation of the growth and the finite amplitude dynamics of rip channels and crescentic sandbars [e.g., *Castelle and Ruessink*, 2011].

2.1.1. Wave Module

[7] The wavefield and resulting radiation stress components are computed from the spectral wave model SWAN [*Booij et al.*, 1999] that solves the spectral wave action balance equation. As depth-induced wave breaking drives nearshore circulation, wave energy dissipation in the surf zone must be accurately computed. We used the parameterization of *Battjes and Janssen* [1978] with the breaker parameter γ_b as proposed by *Battjes and Stive* [1985], here $\gamma_b = 0.73$. These SWAN settings have been extensively validated with field cases [e.g., *Ris et al.*, 1999]. In addition, the reliability of this parameterization to drive nearshore circulation has been proven during low- to moderate-energy wave conditions [*Bruneau et al.*, 2011], which are the conditions considered in our numerical experiments.

2.1.2. Flow Module

[8] The flow model is based on the depth- and phase-averaged nonlinear shallow water equations [*Phillips*, 1977]. The wave group scale forcing [*Reniers et al.*, 2004] is disregarded in the flow model. The vertical structure of the flow was not resolved, despite the potentially significant variation of the velocity profile in rip current settings [e.g., *Haas and Svendsen*, 2002]. These are typical assumptions in nonlinear morphodynamic modeling of 3-D surf zone sandbars [e.g., *Garnier et al.*, 2006]. The nonlinear shallow water equations comprise the water mass conservation and momentum conservation equation that read, using the Einstein summation convention:

$$\frac{\partial Q_i}{\partial t} + \frac{\partial}{\partial x_j}\left(\frac{Q_i Q_j}{h}\right) + gh\frac{\partial \eta}{\partial x_i} + \frac{1}{\rho}\frac{\partial S_{ij}}{\partial x_j} - \frac{1}{\rho}\frac{\partial T_{ij}}{\partial x_j} + \frac{\tau_i^b}{\rho} = 0 \qquad (1)$$

$$\frac{\partial \eta}{\partial t} + \frac{\partial Q_j}{\partial x_j} = 0 \qquad (2)$$

where t is time, h is the mean water depth; $Q_i = hU_i$ is the water volume fluxes with the subscript $_i$ referring to the two horizontal coordinates (with x and y the alongshore and cross-shore axis, respectively), U_i is the wave-driven mass flux velocity according to *Mei* [1989], η is the mean free surface elevation, g is the gravitational acceleration, ρ is the water density, S_{ij} is the radiation stress tensor [*Phillips*, 1977], $\tau_i^b = \rho C_f u_{rms} U_i$ is the bed shear stress, u_{rms} is the

root-mean-square wave orbital velocity at the bottom, C_f is a bottom friction coefficient (equal to 0.0015 in the present study), and T_{ij} is the lateral mixing term which describes the horizontal momentum exchange due to the combined action of turbulence and mean current. Using the formulation proposed by *Battjes* [1975],

$$T_{ij} = \rho h \nu \left(\frac{\partial U_i}{\partial x_j} + \frac{\partial U_j}{\partial x_i} \right) \quad (3)$$

where the eddy viscosity ν is defined as

$$\nu = Mh \left(\frac{D}{\rho} \right)^{1/3} + \nu_0 \quad (4)$$

where D is the rate of energy loss through depth-induced wave breaking; M is a dimensionless coefficient (taken as 5 in the present study) and ν_0 is a constant eddy viscosity (taken as 5 m^2 s^{-1} in the present study). The latter eddy viscosity is used to damp potential hydrodynamic instabilities in the setup and circulation.

[9] In equation (1), the flow is driven by the gradient in radiation stresses S_{ij} of the surface water waves [*Longuett-Higgins and Stewart*, 1964] that read

$$S_{ij} = E \left(\frac{c_g}{c} \frac{k_i k_j}{k^2} + \left(\frac{c_g}{c} - \frac{1}{2} \right) \delta_{ij} \right) \quad (5)$$

where E is the wave energy density defined as $E = \rho g H_{rms}^2/8$; H_{rms} is the root-mean-square wave height; c_g and c are the group and phase velocity using linear wave theory, respectively; k is the wave number; and δ_{ij} is the Kronecker delta. For irregular waves, c, c_g and k are based on the spectral peak period.

2.1.3. Sediment Module

[10] Sediment transport computation is crucial to sandbar evolution as it provides the time-dependent coupling mechanism for adjusting the seabed which, in turn, alters the wavefield and wave-driven currents. Some of the existing sediment transport formulations in nonlinear morphodynamic models result in model blow-up for long-term simulations because the bed slope and bar amplitude become locally too large [e.g., *Drønen and Deigaard*, 2007; *Castelle et al.*, 2010a]. An alternative approach must be used if one wants to run simulations over long durations, i.e., several times the typical 3-D pattern growth time. An efficient and reasonably easy to implement approach is to assume that the cross-shore transport driven by wave nonlinearities and undertow is in balance with the gravitational downslope transport for a given equilibrium cross-shore beach profile Z_f^0 [*Garnier et al.*, 2006, 2008]. In other words, we assume that rip channels evolve more rapidly than the rate at which the beach profile is changing. In addition, as previously done in a number of numerical studies on nearshore bed form formation [e.g., *Falqués et al.*, 2000], we can assume that hydrodynamics plays a dominant role in such a way that accurate and/or complex description of sediment transport [e.g., *Van Rijn*, 1989] is not necessary to give some conceptual insight into the physical mechanisms that govern the bed form dynamics [e.g., *Schielen et al.*, 1993; *Falqués et al.*, 1996]. This type of simplified approach has been previously used in linear stability analysis studies [e.g., *Falqués et al.*, 1996, 2000; *Calvete et al.*, 2005] and more recently in nonlinear stability analysis [e.g., *Garnier et al.*, 2006]. Accordingly, the original sediment transport module [*Castelle et al.*, 2010a] was modified to examine the finite amplitude dynamics. We use a simplified advective sediment flux [*Castelle and Ruessink*, 2011] together with a gravitational downslope sediment transport that causes an increase in morphodynamic diffusivity. The latter produces a damping of the patterns essential for the onset of saturation of the rip channels [e.g., *Garnier et al.*, 2010]. In our model the horizontal sediment flux vector $\vec{Q}_s$ is

$$\vec{Q}_s = \alpha(\overline{\overline{|\vec{u}_b(t)|^3 \vec{u}_b(t)}} - \gamma u_{rms} \vec{\nabla} Z) \quad (6)$$

where α is a stirring factor; γ is a bed slope coefficient and $\vec{u}_b(t) = \vec{U} + (u_{rms} \cos\omega t)\vec{e}_k$ is the total flow velocity at the bottom (mean currents and orbital velocity, here assuming linear waves with ω the wave's angular frequency based on spectral peak) with $\vec{e}_k$ the unit vector along the wave ray (based on spectral peak). The $\overline{\overline{()}}$ notation defines time-averaging over a duration longer than the typical wave period. Finally, Z is the bed level deviation from initial equilibrium, i.e., $Z = Z_f - Z_f^0$, where Z_f and Z_f^0 are the seabed level and the initial equilibrium beach profile, or the basic state, respectively. The first term in equation (6) is the advective part in our sediment transport formula, similar to the suspended sediment load of *Bailard* [1981]. The second term is the downslope sediment transport with respect to the basic state. In the following we set $\alpha = 2.10^{-4}$ s^3 m^{-2} and $\gamma = 100$ m^3 s^{-3}. These settings (for more details, see *Castelle and Ruessink* [2011]) were chosen balancing the desire to both prevent any model blow-up in the range of wave conditions used both by *Castelle and Ruessink* [2011] and herein and to increase the possibility of observing merging and splitting dynamics. Because the advective part in our sediment transport formula is different from that of *Garnier et al.* [2006, 2008, 2010] our reference values of γ and α are not comparable with those of *Garnier et al.* [2006]. Yet, simulated rip channel systems and wave-driven circulations at saturation are similar in patterns and grow over similar timescales.

[11] The new seabed level Z_f was computed every morphological time step using the sediment mass conservation equation:

$$\frac{\partial Z_f}{\partial t} + \frac{1}{1-p} \vec{\nabla} \vec{Q}_s = 0 \quad (7)$$

where $p = 0.4$ is the sediment porosity. The morphological time step for the bed update scheme, which is different from the hydrodynamic time step (1 s), was 1 h throughout. All the simulations were run for 2000 morphological time steps, that is, 83.3 days of morphological evolution. In our model, the shoreline is allowed to evolve, which is a major difference with other nonlinear morphodynamic models applied to 3-D surf zone sandbar behavior. The sediment fluxes are computed at cell centers and further interpolated at the cell interfaces, artificially allowing sediment fluxes to transfer across the interface between dry and wet cells. Even though this is not a real swash zone, this allows the formation of

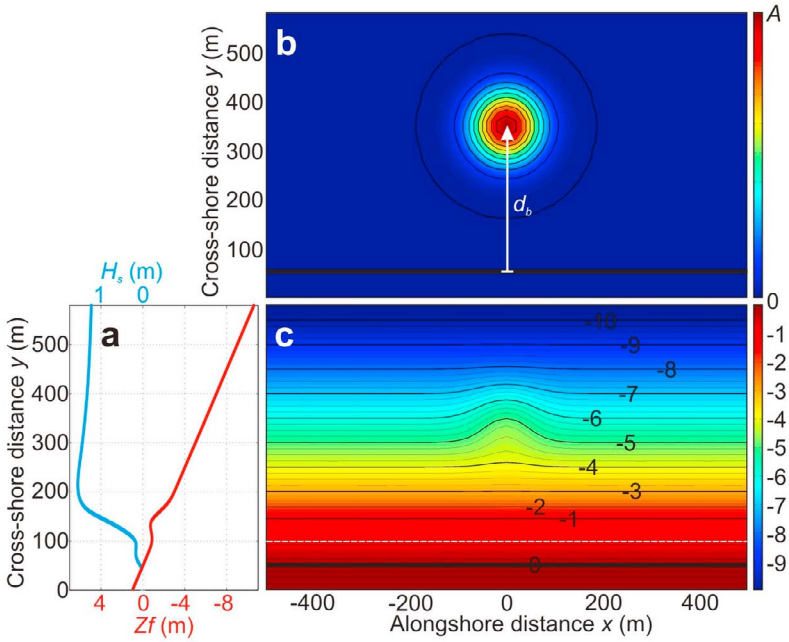

Figure 1. (a) Initial alongshore-uniform beach profile (red) with cross-shore distribution of the significant wave height H_s (H_s = 1.2 m, T_p = 10 s and $\theta = 0°$ at the offshore boundary). (b) Zoom at -500 m < x < 500 m of the superimposed offshore perturbation at a distance d_b from the 0 m sea level shoreline with height A (color bar). (c) Initial bathymetry (basic state) with the white dashed line indicating the location of the alongshore profile Z_b and color bar indicating seabed elevation in meters. In Figures 1b and 1c the thick black line indicates the 0 m sea level shoreline.

shoreline features such as megacusps, which are shoreline signatures of rip current presence.

2.2. Model Setup

[12] We ran the model for a number of different initial single-barred beach bathymetries. The computational grid had an alongshore and cross-shore length of 8000 m and 580 m, respectively, 20 × 20 m grid cells, and periodic lateral boundary conditions whose effect will be discussed later. The basic state consisted of a beach with a 1:50 planar sloping depth profile, with its offshore extent in 10.6 m water depth. A bar was superimposed onto this planar profile, located 90 m from the mean sea level shoreline with its crest in 0.8 m depth (Figure 1a).

[13] First, an alongshore-uniform profile without a bathymetric anomaly was considered. Random perturbations with a magnitude of 1 mm in the seabed were superimposed on the initial alongshore-uniform single-barred beach to excite nearshore instabilities. Hereafter we refer to this initial bathymetry as the alongshore-uniform scenario since there is no preexisting offshore perturbation.

[14] We designed additional initial bathymetries, with the same sandbar characteristics, and with the presence of one offshore bathymetric anomaly. To simplify, the offshore perturbation was described by a two-dimensional Gaussian function at a distance d_b from the 0 m sea level shoreline with a height A (Figure 1b). This perturbation was superimposed on the alongshore-uniform single-barred beach geometry, in the center of the domain at x = 0, to obtain an alongshore nonuniform initial bathymetry (Figure 1c). In our simulations we considered perturbations with -1.5 m ≤ A ≤ 1.5 m to address the influence of both bumps and troughs on the evolution of surf zone rip channels. The offshore bathymetric anomaly was part of the basic state which means that the offshore bump or trough did not significantly flatten or get infilled during the simulations, respectively.

[15] Time-invariant offshore wave conditions were used throughout this study with H_s = 1.2 m and T_p = 10 s. Different values of the offshore wave angle to the shore θ were implemented with $0 \le \theta \le 3.5°$. The simulated rip channel behavior with a preexisting offshore perturbation was very similar for $\theta > 3°$ because of the lateral boundary conditions in the model (this is further discussed in section 4). Therefore simulations with $3.5 < \theta < 7°$ are not presented.

2.3. Model Analysis

[16] Below we detail how we examined surf zone rip channel behavior. First, we used a global analysis of beach evolution (section 2.3.1) to both detect the linear, nonlinear and saturation regimes of rip channels and to quantify rip channel alongshore migration downdrift and updrift of the offshore perturbation. Second, we used a wavelet analysis (section 2.3.2) to estimate updrift and downdrift rip spacing. Finally, the offshore bathymetric anomaly control on surf zone rip currents and resulting initial rip channel formation was examined (section 2.3.3) to explain the contrasting updrift/downdrift rip channel behavior in section 4.

2.3.1. Global Analysis

[17] To examine the evolution of rip channels, a 'global analysis' of beach evolution [*Garnier et al.*, 2006, 2010] was

used. This consists of analyzing variables that are integrated over the whole computational domain. The notation $\overline{()}^{g}$ is introduced to define an average over the computational domain which, for a given function $f = f(x, y, t)$, reads

$$\bar{f}^{g} = \frac{1}{L_x L_y}\int_0^{L_x}\int_0^{L_y} f\,dxdy \tag{8}$$

where L_x and L_y are the longshore and cross-shore length of the computational domain, respectively. In addition, because simulations comprising an offshore bathymetric anomaly showed that rip channels often possess remarkably contrasting behavior updrift ($x < 0$) of the perturbation with respect to downdrift ($x > 0$), we discriminated the global analysis updrift of the perturbation ($-3000\ \mathrm{m} \le x \le -1000\ \mathrm{m}$) and downdrift of the perturbation ($1000\ \mathrm{m} \le x \le 3000\ \mathrm{m}$) with the $\bar{.}^{u}$ and $\bar{.}^{d}$ notations:

$$\bar{f}^{u} = \frac{1}{2000 L_y}\int_{-3000}^{-1000}\int_0^{L_y} f\,dxdy \tag{9}$$

$$\bar{f}^{d} = \frac{1}{2000 L_y}\int_{1000}^{3000}\int_0^{L_y} f\,dxdy \tag{10}$$

[18] Using the same definition as *Garnier et al.* [2010], the global growth rate, σ^{i} ($i = g$ for the whole computational domain, u for the updrift or d for the downdrift), is given by

$$\sigma^{i} = \frac{1}{2\|Z\|^{i2}}\frac{d}{dt}\left(\|Z\|^{i2}\right) \tag{11}$$

where $\| Z \|^{i}$ is the L_2 norm of Z:

$$\|Z\|^{i} = \sqrt{\overline{Z^2}^{i}} \tag{12}$$

so that $\| Z \|^{i}$ is a measure of beach three dimensionality.

[19] An additional variable that is considered in this study is the instantaneous global longshore migration rate V_L^{i} of the rip channels. According to *Vis-Star et al.* [2008], V_L^{i} is defined as

$$V_L^{i} = -\frac{1}{\overline{(\partial Z/\partial x)^2}}\overline{\frac{\partial Z}{\partial x}\frac{\partial Z}{\partial t}}^{i} \tag{13}$$

[20] Because of the periodic lateral boundary conditions implemented in the model, downdrift rip channels eventually enter the updrift domain for $\theta > 0°$. When running a simulation for a long duration and significant rip channel alongshore migration, V_L^{u} and V_L^{d} eventually become inseparable. Therefore, to have a good measure of the updrift and downdrift rip channel migrations, we computed V_L^{u} and V_L^{d} when $\sigma^{g} \approx 0$ for the first time. *Garnier et al.* [2010] called the corresponding state the saturated state. Therefore here we defined the saturation time t_s as the time when for the first time $\sigma^{g} < 0.01\ \mathrm{d}^{-1}$. Because the detection of the saturation time was sometimes complicated for situations with an offshore bathymetric anomaly (large variability of σ^{g} close to the expected t_s as a result of merging of rips at $x \approx 0$), we defined the saturation time from the corresponding alongshore-uniform scenario simulation. Hereafter, updrift and downdrift rip channel longshore migration rates at saturation ($t = t_s$) are noted $\tilde{V}_L^{u}$ and $\tilde{V}_L^{d}$, respectively.

2.3.2. Rip Spacing

[21] The alongshore profile $Z_b(x, t) = Z_f(x, y = 100\ \mathrm{m}, t)$ between the bar crest and the mean sea level shoreline (Figure 1c) was computed at every time step to estimate rip channel time evolution. This location is considered to be representative of the rip channel evolution. Because simulations with preexisting offshore perturbation often showed large variability in rip channel alongshore scales, the traditional Fourier Transform was not suitable to estimate rip spacing. Instead, we used a wavelet analysis to examine the evolution of rip channels and how rip spacing varies alongshore. Using the toolbox wtc-r14 [*Jevrejeva et al.*, 2003; *Grinsted et al.*, 2004], we applied the continuous wavelet transforms $W_n^{z}(s)$ defined as the convolution of a discrete sequence z_n ($n = 0, \ldots, N-1$) with a scaled and normalized mother wavelet function ψ_0:

$$W_n^{z}(s) = \left(\frac{\mathrm{d}z}{s}\right)^{1/2}\sum_{n'=0}^{N-1} z_{n'}\psi_0^{*}\left(\frac{(n'-n)\mathrm{d}z}{s}\right) \tag{14}$$

where $\mathrm{d}z$ is the uniform spacing in z_n, n is the alongshore coordinate, s is the alongshore scale [*Torrence and Compo*, 1998], and the asterisk is the complex conjugate. The $W_n^{z}(s)$ is used to decompose Z_b into energy at a given alongshore scale and at a given alongshore distance. This enables both the detection of the dominant spatial modes of variability and how these modes vary in space. As in some previous wavelet applications to sandbar data [e.g., *Ruessink et al.*, 2007; *Castelle et al.*, 2010b], we used the Morlet wavelet ψ_0 because of its good localization characteristics in both the space and frequency domains. In all results below, the term wavelength refers to the Fourier wavelength λ equivalent to the wavelet scale s. We determined the statistical significance of $W_n^{z}(s)$ against synthetic red noise series, as detailed by *Torrence and Compo* [1998]. The edge-affected part of $W_n^{z}(s)$ is termed the cone of influence (COI).

[22] We additionally computed the spatial averages (outside of the COI) of $W_n^{z}(s)$ updrift of the offshore bathymetric anomaly $\overline{W^{z}}^{u}(s)$ and downdrift of the perturbation $\overline{W^{z}}^{d}(s)$. As for the alongshore rip channel migrations rates, V_L^{u} and V_L^{d}, downdrift rip channels eventually enter the updrift domain and the downdrift rip spacing can be progressively disturbed by the downdrift rip spacing. Therefore, we selected the wavelet transform at the end of the saturation process ($t = t_s$) and we computed the corresponding updrift and downdrift spatial averages $\widetilde{W^{z}}^{u}(s)$ and $\widetilde{W^{z}}^{d}(s)$. The wavelengths for which $\widetilde{W^{z}}^{u}(s)$ and $\widetilde{W^{z}}^{d}(s)$ are maximum define the updrift rip spacing $\tilde{\lambda}_m^{u}$ and downdrift rip spacing $\tilde{\lambda}_m^{d}$ at saturation.

2.3.3. Offshore Bathymetric Anomaly Control on Surf Zone Rip Currents and Resulting Initial Rip Channel Formation

[23] The impact of wave transformation across the offshore perturbation on the generation of inshore rip currents was addressed with two approaches: the traditional radiation stress approach and the more recently introduced vorticity forcing term related to spatial gradients in depth-induced

breaking wave dissipation. The motivation for combining these two approaches is twofold: (1) to address in detail the nearshore wave-induced circulations across the sandbar due to wave refraction offshore and (2) to test the ability of the vorticity conservation equation to provide straightforward quantitative information of the strength and rotational nature of wave-driven circulations without the requirement of running a wave-driven circulation model.

[24] It is commonly stated that alongshore pressure gradients $-\rho g \partial\eta/\partial x$ drive rip current circulations. However, the major driving mechanism for nearshore circulation currents is the combination of the radiation stress gradients $\vec{F}_w$ and the pressure gradients $\vec{F}_p$ [*Haas and Svendsen*, 2002; *Castelle and Bonneton*, 2006]. Thus, the vectorial sum of the two components, that we can derive from equation (1), indicates how much net forcing is available to drive nearshore currents only and reads

$$F_{ri} = -gh\frac{\partial \eta}{\partial x_i} - \frac{1}{\rho}\frac{\partial S_{ij}}{\partial x_j} \tag{15}$$

[25] The second approach is based on the differential broken wave energy dissipation derived from the depth-integrated and time-averaged momentum equations given by *Smith* [2006]. The resulting advection-diffusion mean flow vertical vorticity conservation equation is [*Bonneton et al.*, 2010; *Bruneau et al.*, 2011]

$$\frac{\partial \Gamma}{\partial t} + \vec{\nabla}.(\Gamma \vec{U}) = \left(\vec{\nabla} \wedge (D\vec{e}_k)\right)\cdot\vec{e}_z + \tau_t \tag{16}$$

where $\Gamma = \left(\vec{\nabla} \wedge \vec{U}\right)\cdot\vec{e}_z$ is the mean vertical vorticity; $\vec{e}_z$ is the vertical unit vector; $D = D_b k/\sigma_r$ is the intensity of the depth-induced breaking dissipative force [*Bonneton et al.*, 2010] with D_b the depth-induced wave breaking dissipation; σ_r is the relative frequency (all based on spectral peak) and τ_t the turbulent diffusion of the vorticity. For quasi-stationary rip current circulations ($\partial\Gamma/\partial t \approx 0$), the nonlinear advective term $\vec{\nabla}.(\Gamma\vec{U})$ becomes small in comparison with $\left(\vec{\nabla} \wedge (D\vec{e}_k)\right)\cdot\vec{e}_z$ [*Bruneau et al.*, 2011]. This results in a balance between the spatial gradients in broken wave energy dissipation, and the turbulent diffusion of the vorticity $\tau_t \sim \nu_t\vec{\nabla}^2\Gamma$ where ν_t is a turbulent eddy viscosity. Therefore the strength and rotational nature of nearshore circulations are essentially governed by the wave-induced vorticity forcing term F_v that reads

$$F_v = \left(\vec{\nabla} \wedge (D\vec{e}_k)\right)\cdot\vec{e}_z \tag{17}$$

3. Results

3.1. No Perturbation Versus Perturbation

[26] Below we address two simulations with the same wave conditions (H_s = 1.2 m, T_p = 10 s and θ = 1.5°) but contrasting offshore geometries: the alongshore-uniform scenario (no offshore perturbation) and an alongshore non-uniform scenario characterized by an offshore perturbation with $A = -1$ m (trough) and d_b = 350 m. The latter will be hereafter referred to as the reference case simulation. The same approach was systematically used for all the other simulations from which results are synthesized in section 3.2.

3.1.1. General Behavior

[27] Figure 2 shows the time evolution of the alongshore profile Z_b and corresponding time series of σ^i, $\|Z\|^i$ and V_L^i (i = g, u, d) for the two simulations. For the alongshore-uniform scenario (Figures 2a, 2c, and 2e), the rips appear at $t \approx$ 5–6 days (Figure 2a) with concurrent exponentially increasing $\|Z\|^g$ and highest values of σ^g (Figure 2c). This characterizes the linear regime [*Garnier et al.*, 2010]. From about day 6 to day 10, σ^g strongly decreases with merging of rips and less rapidly increasing $\|Z\|^g$ (Figure 2c). This characterizes the saturation process [*Garnier et al.*, 2010]. Further mergings occur for t > 10 days ($\sigma^g \approx 0$, saturated state) as rips tend to self-organize into more regularly spaced features. For t > 20 days no further rip merging occurs and the rip channel alongshore migration rate stabilizes at $V_L^g \approx 16$ m d^{-1} (Figure 2e). Considering the reasonably small angle of incidence (θ = 1.5°), 16 m d^{-1} is high. The systematic overestimation of rip channel migration rates with nonlinear morphodynamic models has already been pointed out by *Falqués et al.* [2008]. In nature, similar migration rates have been observed only for much higher angle of incidence [e.g., *Van Enckevort and Ruessink*, 2003]. For the alongshore-uniform scenario the saturation time is t_s = 9.37 days.

[28] This rip channel behavior contrasts with that in the experiment with the preexisting offshore bathymetric anomaly (Figures 2b, 2d, and 2f). Within 1–2 days, a rip channel forms shoreward of the perturbation at $x \approx 0$ (Figure 2b). At t = 2 days a second rip channel forms updrift with a third one later at $t \approx 5$ days. Downdrift of the perturbation, rip channels form at $t \approx 4$ and 6 days at $x \approx 900$ m and 1800 m, respectively. In the meantime, rips appear at $x < -1000$ m and $x > 3000$ m from about t = 5–6 days (Figure 2a) with concurrent exponentially increasing $\|Z\|$ and highest values of σ^g (Figure 2d). This is similar to the rip channel behavior in the alongshore-uniform scenario. The latter rip channel formation is not affected by the offshore bathymetric anomaly and these rip channels are hereafter referred to as free rip channels (indicated by white circles in Figure 2b). Downdrift of the perturbation, for t > 10 days, rip channels progressively migrate downdrift at a rate 4 m d^{-1} < V_L^d < 10 m d^{-1} (Figure 2f) which is significantly smaller than for the alongshore-uniform scenario. In addition, the downdrift mean rip spacing is larger than for the alongshore-uniform scenario (Figure 2b). In contrast, updrift of the perturbation for 10 days < t < 60 days, rip channels progressively migrate downdrift at a rate 20 m d^{-1} < V_L^u < 23 m d^{-1}. For t > 60 days V_L^u subsequently decreases (Figure 2f) as the downdrift rip channels progressively enter the updrift domain (Figure 2b). All the updrift rip channels continuously merge to the forced rip channel shoreward of the offshore perturbation at x = 0 with no updrift rip channel entering the downdrift domain throughout the simulation.

[29] This alongshore nonuniform simulation (Figures 2b, 2d, and 2f) illustrates the difficulty of discriminating updrift and downdrift domains when running a simulation over a long duration (downdrift rip channels eventually enter the updrift domain). To more accurately address the downdrift and updrift rip channel behavior, we analyzed rip channels at the saturation time t_s when both forced and free rip channels

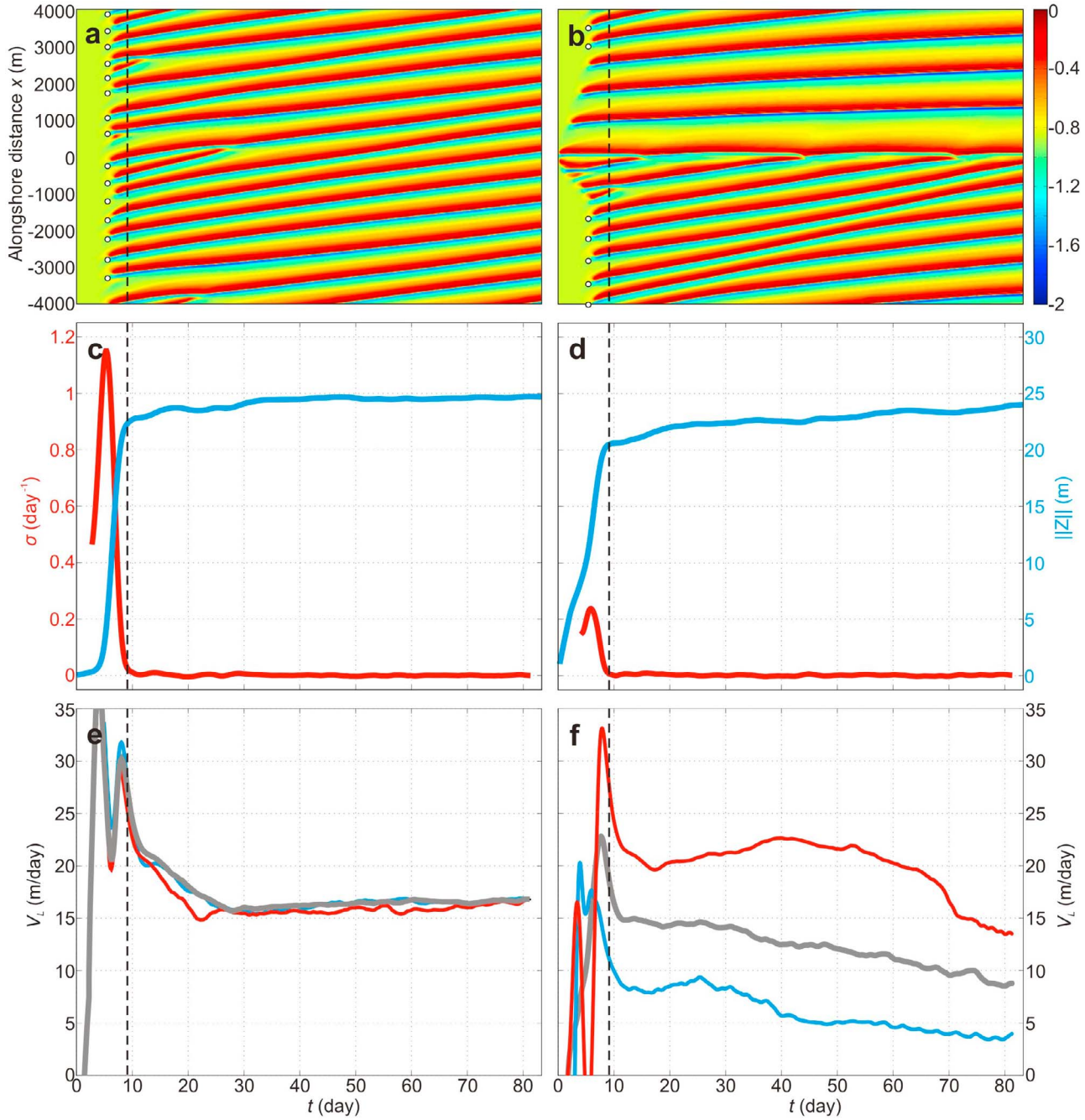

Figure 2. Formation and subsequent nonlinear evolution of rip channels for H_s = 1.2 m, T_p = 10 s and θ = 1.5° starting (left) from an alongshore-uniform beach and (right) with an offshore perturbation at x = 0 with A = −1 m (trough) and d_b = 350 m (reference case simulation). (a and b) Time evolution of the alongshore profile Z_b with white circles indicating the formation of free rip channels at $t \approx 6$ days and corresponding time series of (c and d) global growth rate σ^g (red) and $\|Z\|^g$ (blue) and (e and f) global longshore migration rate V_L^g (gray), updrift migration rate V_L^u (red) and downdrift migration rate V_L^d (blue). The vertical dashed line indicates the saturation time t_s = 9.37 days.

saturate and updrift rip channels are unlikely to affect/be affected by downdrift rips.

3.1.2. Configuration at Saturation Time t_s

[30] In this section we analyze the alongshore nonuniform scenario (Figures 2b, 2d, and 2f) at the saturation time (Figure 3). Figure 3a shows the alongshore profile Z_b at t_s = 9.37 days. The alongshore nonuniform variability of the seabed along Z_b has a typical height of 1.2–1.4 meters. The local wavelet spectrum for this situation indicates that Z_b contains alongshore nonuniform statistically significant power (Figure 3b) with larger wavelengths at 1000 m < x < 3000 m (downdrift domain in red in Figure 3b) than at −3000 m < x < −1000 m (updrift domain in blue in Figure 3b). The alongshore-averaged local wavelet spectra

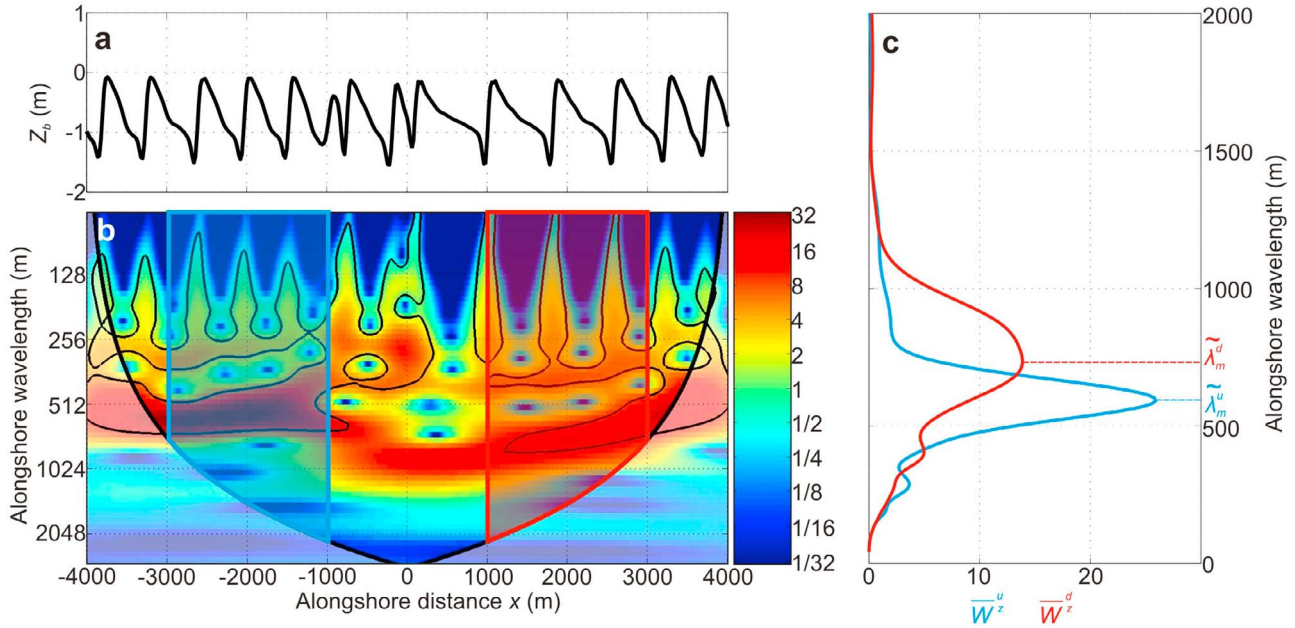

Figure 3. (a) Alongshore profile Z_b at the saturation time t_s = 9.37 days for H_s = 1.2 m, T_p = 10 s and θ = 1.5° starting from the alongshore nonuniform reference case with an offshore perturbation at x = 0 with A = −1 m (trough) and d_b = 350 m (reference case simulation). (b) Corresponding local wavelet spectrum $W_n^z(s)$ normalized by the variance with the 5% significance level against red noise (thick black contours), the cone of influence (COI) (shaded white area), superimposed areas to compute the updrift and downdrift local wavelet spatial averages $\overline{W^z}^u(s)$ and $\overline{W^z}^d(s)$ in blue and red, respectively, excluding local wavelet values within the COI. (c) Resulting $\overline{W^z}^u(s)$ and $\overline{W^z}^d(s)$ and updrift and downdrift mean rip spacing $\widetilde{\lambda}_m^u$ = 525 m and $\widetilde{\lambda}_m^d$ = 742 m defined as the wavelength for which $\overline{W^z}^u(s)$ and $\overline{W^z}^d(s)$ are maximum at the saturation time t_s in blue and red, respectively.

of Z_b in the updrift domain $\widetilde{W^z}^u(s)$ and downdrift domain $\widetilde{W^z}^u(s)$ are shown in blue and red in Figure 3c, respectively. Results show that the sandbar contains statistically high power at $\widetilde{\lambda}_m^u$ = 525 m (mean updrift rip spacing) and at $\widetilde{\lambda}_m^d$ = 742 m (mean downdrift rip spacing).

[31] The presence of the localized peaks of statistically significant power in Figure 3 is in line with our definition of the downdrift (1000 m < x < 3000 m) and updrift (−3000 m < x < −1000 m) domains. In Figure 3b there is a reasonably alongshore nonuniform statistically significant power in the downdrift domain at 1000 m < x < 3000 m and a lack of statistically significant power at −1000 m < x < 0 because rips were merging updrift of the offshore bathymetric anomaly at this time of the simulation. This was rarely the case for the other simulations.

3.1.3. Wave-Driven Circulations and Rip Channel Morphology Beyond Saturation Time t_s

[32] To address downdrift and updrift rip channel morphology and wave-driven circulations, we analyze results at t = 30 days when downdrift rip channels had not yet entered the updrift domain yet. Figure 4 shows a zoom at −2000 m < x < 2000 m of the beach morphology with superimposed wave-driven circulations at t = 30 days for the two scenarios described in Figure 2. For the alongshore-uniform scenario (Figure 4a) rip channels are reasonably regularly spaced alongshore. All the rip channels have a similar shape with a deep and narrow, slightly downdrift skewed neck, and a well-developed rip head bar. Megacusps with a cross-shore amplitude of about 40–50 m are also coupled to the rip channel geometry. These alongshore (O(100 m)) and cross-shore (O(10 m)) scales of megacusps are similar to observations of well-developed bar and rip morphologies [e.g., *Wright and Short*, 1984; *Thornton et al.*, 2007]. The undulations of the bathymetric lines coupled to the bar and rip morphology reach into about Z_f = −6 m. Even though large and detailed bathymetric surveys of well-developed 3-D surf zone sandbars are scarce, there is plenty of evidence that undulations (in the form of either isolated shoals or crescentic sandbars) at water depths of about −6 m are common. For example, *Almar et al.* [2010] measured bathymetric undulations at about Z_f = −9 m coupled to a crescentic sandbar with its crest in about 3 m depth. Similar observations were made at sites exhibiting bar and rip morphologies or crescentic sandbars [e.g., *Wijnberg and Kroon*, 2002; *Bender and Dean*, 2003]. The megacusps have a significantly skewed shape (Figure 4a). To date, the two most comprehensive studies on megacusps were done by *Thornton et al.* [2007] and *Orzech et al.* [2011]. They both addressed megacusps along the southern Monterey Bay (California), which is characterized by persistent near-normal wave incidence due to strongly refracted waves and narrow bay aperture. This results in relatively stationary, shore-normal, rip channels. Accordingly, the authors could not address the impact of wave incidence on the shape of megacusps in the presence of migrating and skewed rip channels. Wave-driven rip current circulations are typical in patterns with alongshore feeder currents, a reasonably

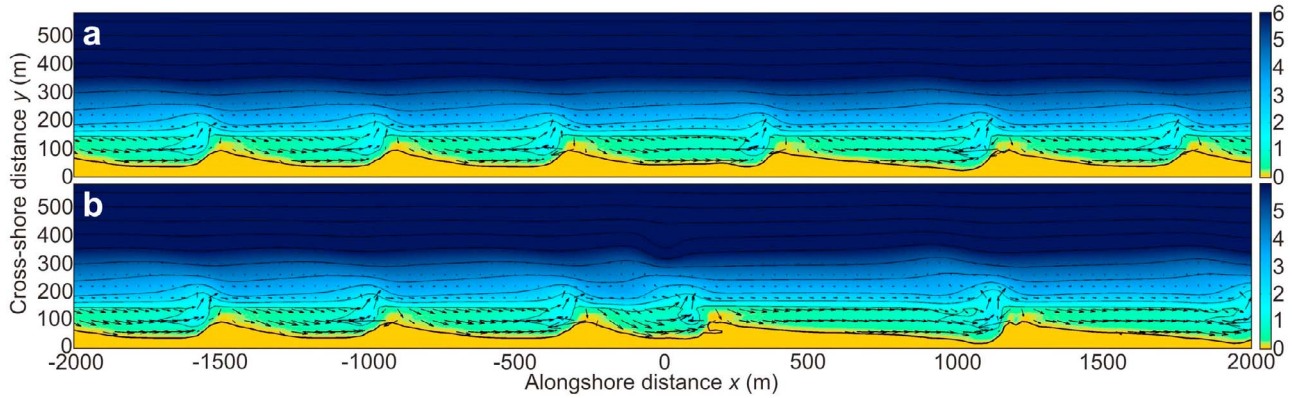

Figure 4. Zoom of the bathymetry at -2000 m $< x <$ 2000 m and $0 < y <$ 300 m with superimposed wave-induced currents (arrows, one out of two vectors are plotted in both directions) at t = 30 days for waves with H_s = 1.2 m, T_p = 10 s and θ = 1.5° (a) starting from the alongshore-uniform beach and (b) starting from the alongshore nonuniform reference case with an offshore perturbation at x = 0 with $A = -1$ m (trough) and d_b = 350 m (reference case simulation). Note the larger rip spacing and more erosive megacusps downdrift of the perturbation than updrift of the perturbation. Color bars indicate seabed elevation in meters, and isobaths (1 m intervals) are contoured in the background.

intense (≈ 0.7 m s^{-1}) and narrow offshore-directed jet in the channel, onshore-directed flow across the shoals and counterrotating cells to the left and right of each rip current. These rip channel morphology and wave-driven hydrodynamics are essentially similar to field and laboratory observations of well-developed bar and rip systems exposed to low- to moderate-energy waves with normal to near-normal incidence [e.g., *Bruneau et al.*, 2009; *Austin et al.*, 2010; *Castelle et al.*, 2010c].

[33] The same applies for the alongshore nonuniform scenario (reference case simulation) at t = 30 days in Figure 4b. As previously shown (Figure 2b), rip spacing is substantially larger downdrift of the offshore bathymetric anomaly than updrift. In addition, rip currents are more shore-normal downdrift of the offshore perturbation than updrift (Figure 4b). Megacusps show alongshore-variable cross-shore scales for the alongshore nonuniform scenario (Figure 4b). Updrift of the offshore perturbation, megacusps have a cross-shore amplitude of about 40–50 m, similar to the alongshore-uniform scenario, while megacusps systematically have a larger cross-shore amplitude of about 60–70 m downdrift of the perturbation (Figure 4b).

3.2. Influence of Perturbation Height, Wave Angle and Offshore Perturbation Distance to the Shore on Surf Zone Rip Channel Evolution

[34] Below we address the influence of the perturbation height A, wave angle θ and offshore perturbation distance to the shore d_b on the formation and subsequent evolution of rip channels. First, we describe the general evolution of the rip channels throughout the simulations for different values of d_b. Second, we set d_b = 350 m and investigate the influence of A and θ on rip spacing and migration rate at saturation time t_s.

3.2.1. General Behavior

[35] Figure 5 shows the time evolution of the alongshore profile Z_b for waves with H_s = 1.2 m, T_p =10 s and θ = 1.5° for an offshore trough with $A = -1$ m and different offshore distances to the shore d_b = 350 m (in about 6 m depth, reference case simulation), 450 m (in about 8 m depth) and 550 m (in about 10 m depth). Results show that, for d_b = 350 m and 450 m, rip channel evolution is similar up to $t \approx$ 30 days (Figures 5a and 5b) as the forced rip channel shoreward of the offshore bathymetric anomaly at $x \approx 0$ does not enter the downdrift domain. Downdrift mean rip spacing and longshore migration rates are about 800 m and 10 m d^{-1}, respectively. For $t >$ 30 days, the forced rip channel enters the downdrift domain for d_b = 450 m (Figure 5b). These two situations contrast with that for d_b = 550 m (Figure 5c), with updrift rip channels continuously entering the downdrift domain. Downdrift rip channels still have a larger mean spacing (about 800 m) than updrift rip channels until $t \approx$ 30 days when updrift and downdrift rip channels become inseparable. Similar results were obtained for an offshore trough. Overall, for a given A, the influence of the presence of an offshore bathymetric anomaly on surf zone rip channels decreases with increasing distance to the shore of the perturbation. In the following we only address situations with d_b = 350 m.

[36] Figure 6 shows the time evolution of the alongshore profile Z_b to address the influence of the presence of an offshore trough ($A = -0.5$ m, -1 m and -1.5 m at x = 0 with d_b = 350 m) on the surf zone rip channels for different wave angles to the shore θ (0°, 1°, 2° and 3°). For shore-normal waves (θ = 0°, Figures 6a–6c) a rip channel systematically forms within a few morphological time steps shoreward of the offshore trough at x = 0. Within a few days, further rip channels progressively form on both sides of the forced rip channel. Later for t = 5–10 days, free rip channels form farther away from the offshore trough (Figures 6a–6c). Overall for shore-normal waves, mean rip spacing is not overly affected by the offshore trough aside from triggering the formation of a "forced" rip (at x = 0).

[37] Rip channel behavior is more complicated for waves with oblique incidence (Figures 6d–6l). If the offshore wave angle to the shore θ is reasonably small and/or the trough

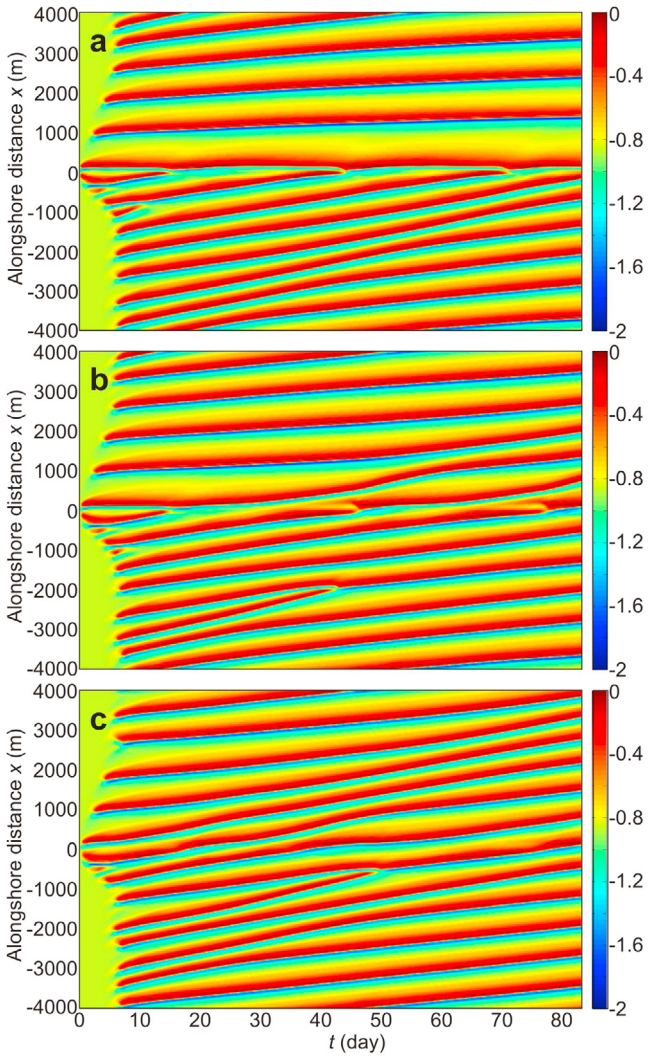

Figure 5. Influence of the offshore perturbation distance to the shore d_b on the formation and subsequent nonlinear evolution of rip channels. The offshore perturbation consists of an offshore trough with $A = -1$ m at $x = 0$. Figures 5a–5c show the time evolution of the alongshore profile Z_b with the color bar indicating seabed elevation in meters for H_s = 1.2 m, T_p = 10 s and $\theta = 1.5°$: (a) d_b = 350 m (reference case simulation), (b) d_b = 450 m and (c) d_b = 550 m.

amplitude $|A|$ is large, then updrift rip channels continuously merge to the forced rip channel at $x = 0$ without entering the downdrift domain (Figures 6e, 6f and 6i, see also Figure 2b). For these situations, rip channel behavior is similar to the alongshore nonuniform scenario described in detail in section 3.1. Updrift rip channels are not affected by the offshore perturbation until downdrift rip channels enter the updrift domain at the end of the simulation for $\theta = 1°$ (Figures 6e and 6f) and earlier for $\theta = 2°$ at $t \approx 30$ days (Figure 6i). Downdrift of the bathymetric anomaly, once formed, rip channels progressively migrate downdrift at a lower rate than updrift. In addition, in these numerical experiments, the downdrift mean rip spacing is systematically larger than the updrift mean rip spacing.

[38] For larger θ and/or smaller trough amplitude $|A|$ (Figures 6d, 6g, and 6h), updrift free rip channels continuously or sporadically enter the downdrift domain. In addition, a forced rip channel shoreward of the perturbation at $x = 0$ is not always present. Downdrift, mean rip spacing and alongshore migration rates are larger and smaller than updrift, respectively (Figures 6d, 6g, and 6h), similar to the situations with smaller θ and/or larger trough amplitude $|A|$ (Figure 6e, 6f and 6i). Further increasing θ and/or decreasing trough amplitude $|A|$ (Figures 6g, 6j, 6k and 6l) results in updrift rip channels continuously entering the downdrift domain without remaining at $x = 0$ for a long duration. In this case, for $\theta = 3°$ (Figures 6j, 6k, and 6l), updrift and downdrift rip channels are inseparable, which is a limitation due to the lateral periodic boundary conditions in the model. All the simulations with $\theta > 3°$ showed the same rip channel behavior.

[39] Figure 7 shows the time evolution of the alongshore profile Z_b to address the influence of the presence of an offshore bump (A = 0.5 m, 1 m and 1.5 m) on the surf zone rip channels for the same wave conditions as in Figure 6. For the shore-normal wave forcing (Figures 7a–7c), overall, rip channels behave the same as for an offshore trough with the same amplitude (Figures 6a–6c), as mean rip spacing is not readily affected by A. In contrast to the situations with an offshore trough, however, a bar forms at $x = 0$ instead of a rip channel for shore-normal waves. The situation with A = 1.5 m is more complicated as the two nearby rips almost merge at $x = 0$ from $t \approx 20$ days to the end of the simulation.

[40] For waves with oblique incidence (Figures 7d–7l), a shoal forms rapidly at $x = 0$ and subsequently migrates downdrift with a rip channel progressively forming immediately updrift at about $x \approx 0$. Therefore, morphology at $x \approx 0$ is reasonably similar for an offshore trough and an offshore bump (Figure 6d–6l). However, for the same perturbation amplitude $|A|$, updrift rip channels migrate more easily beyond the $x \approx 0$ position for an offshore bump than for an offshore trough (Figure 7d–7l). Overall, mean rip spacing and rip channel alongshore migration rate are larger and smaller downdrift of the offshore bump than updrift.

3.2.2. Configuration at Saturation Time t_s

[41] As indicated in section 3.1, investigating rip channels at saturation time t_s is relevant to more accurately address the downdrift and updrift rip channel behavior, as updrift rip channels are unlikely to be affected by downdrift rips (and potentially the other way around). Figure 8 shows the updrift and downdrift mean rip spacing $\widetilde{\lambda}_m^u$ and $\widetilde{\lambda}_m^d$ (Figures 8b and 8c) and longshore migration rate $\widetilde{V}_L^u$ and $\widetilde{V}_L^d$ (Figures 8d and 8e), respectively, at saturation time t_s. In agreement with existing linear and nonlinear stability analysis studies [e.g., *Garnier et al.*, 2008], t_s increases with increasing θ (Figure 8a). Mean rip spacing in the downdrift domain (Figure 8c) increases with increasing θ and is systematically larger than both the updrift (Figure 8b) and the alongshore-uniform scenario (Figures 8b and 8c for $A = 0$). In addition, in the downdrift domain for a given θ, mean rip spacing substantially increases with increasing perturbation amplitude $|A|$ (Figure 8c). In contrast, in the updrift domain, mean rip spacing is weakly influenced by θ or A as, overall, rip spacing only very slightly increases with increasing θ with a larger sensitivity for offshore troughs ($A < 0$ in Figure 8b) than for offshore bumps. In the updrift

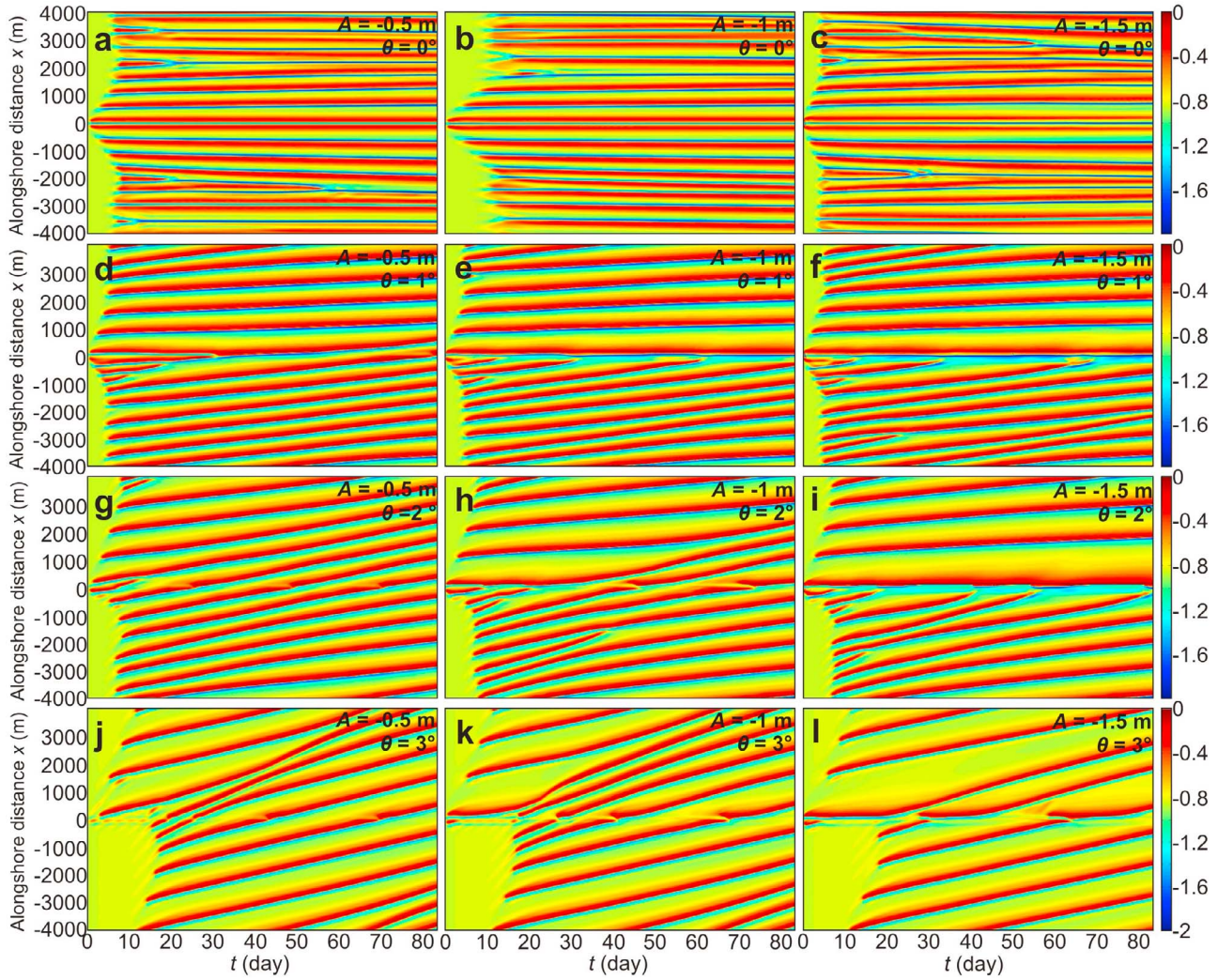

Figure 6. Influence of an offshore trough ($A < 0$) at $x = 0$ with $d_b = 350$ m on the formation and subsequent nonlinear evolution of rip channels. Figures 6a–6l show the time evolution of the alongshore profile Z_b with the color bar indicating seabed elevation in meters for $H_s = 1.2$ m, $T_p = 10$ s. (left) For $A = -0.5$ m, (middle) for $A = -1$ m and (right) for $A = -1.5$ m, with (a, b, c) $\theta = 0°$, (d, e, f) $\theta = 1°$, (g, h, i) $\theta = 2°$ and (j, k, l) $\theta = 3°$.

domain rip channel longshore migration rate increases with increasing θ and is not readily influenced by A (Figure 8d). In contrast, in the downdrift domain (Figure 8e), on the one hand $\widetilde{V}_L^d$ increases with increasing θ and on the other hand $\widetilde{V}_L^d$ decreases with increasing $|A|$ for a given θ. Therefore, for these obliquely incident wave numerical experiment, rip channel alongshore migration rate downdrift of an offshore bathymetric anomaly is systematically smaller than in the alongshore-uniform scenario.

[42] These results are synthesized in Figure 9 that shows the mean rip spacing $\widetilde{\lambda}_m$ versus rip channel migration rate $\widetilde{V}_L$ at saturation time t_s discriminating between the updrift and downdrift behavior. For a given domain (updrift or downdrift, or the whole domain if considering the alongshore-uniform scenario), rip channel migration rate $\widetilde{V}_L$ increases with increasing mean rip spacing $\widetilde{\lambda}_m$. In the downdrift domain, the alongshore migration rate increases with increasing mean rip spacing much more slowly than for both the alongshore-uniform scenario and the updrift domain.

4. Discussion

[43] In this section, we first discuss the links between the initial wave-driven circulations with the subsequent evolution of the rip channels. Second, we qualitatively compare our results with observations at a beach with a persistent offshore trough. We further discuss model limitations and the implications of our modeling exercise.

4.1. Physical Mechanism

[44] We first describe the hydrodynamics and resulting sediment transport patterns at $t = 0$ for different situations to examine the strength and patterns of rip current circulations enforced by wave refraction across the offshore bathymetric anomaly as a function of A and d_b. Second, we examine the time evolution of the hydrodynamics for the reference case

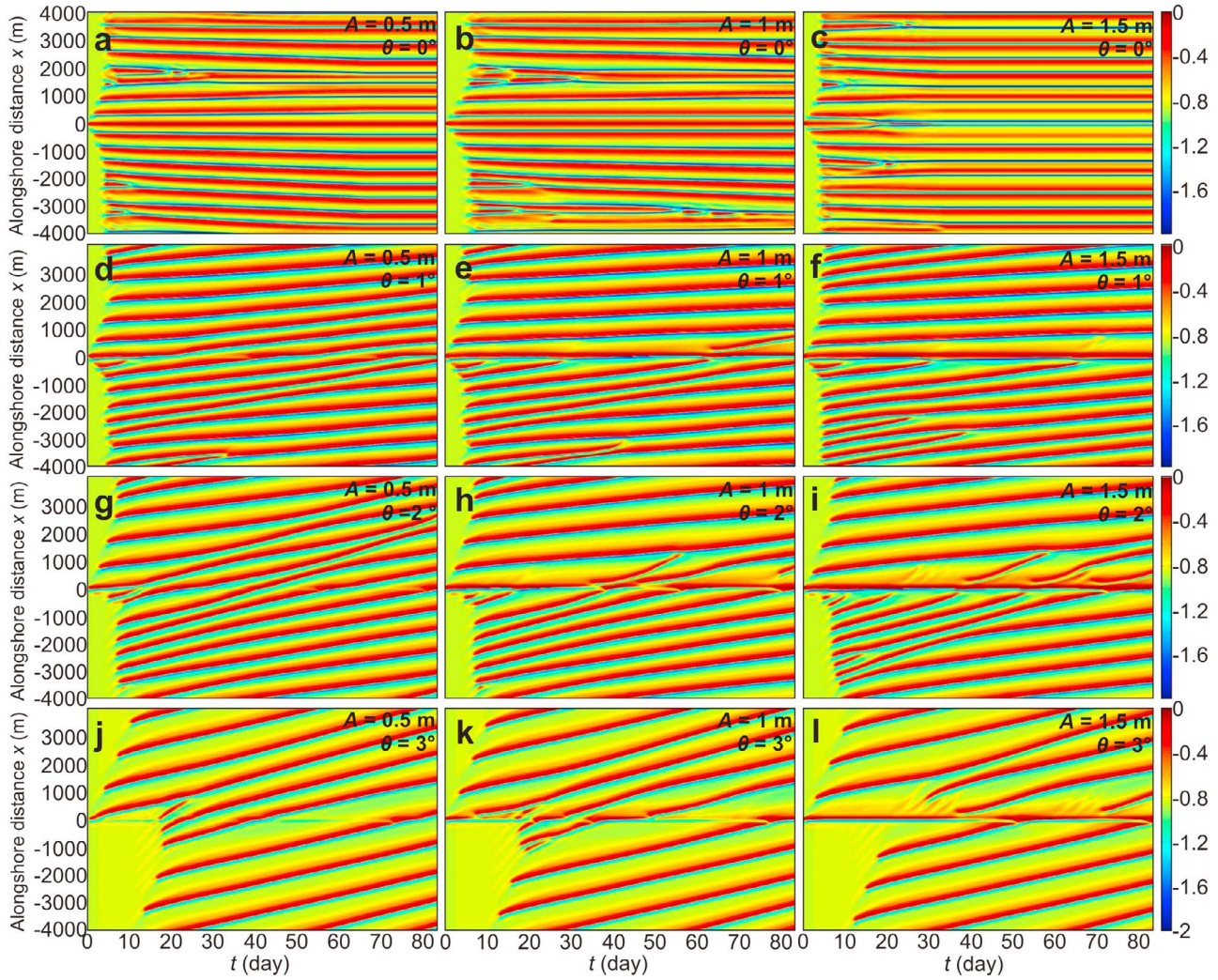

Figure 7. Influence of an offshore bump ($A > 0$) at $x = 0$ with $d_b = 350$ m on the formation and subsequent nonlinear evolution of rip channels. Figures 7a–7l show the time evolution of the alongshore profile Z_b with the color bar indicating seabed elevation in meters for $H_s = 1.2$ m, $T_p = 10$ s. (left) For $A = 0.5$ m, (middle) for $A = 1$ m and (right) for $A = 1.5$ m, with (a, b, c) $\theta = 0°$, (d, e, f) $\theta = 1°$, (g, h, i) $\theta = 2°$ and (j, k, l) $\theta = 3°$.

simulation to explore why updrift and downdrift rip channels behave differently.

4.1.1. Initial Wave-Driven Circulations

[45] Figure 10 shows the hydrodynamics and sediment transport patterns at $t = 0$ for offshore waves with $H_s = 1.2$ m, $T_p = 10$ s and $\theta = 1.5°$ for two alongshore nonuniform configurations with an offshore perturbation at $x = 0$ and $d_b = 350$ m with $A = -1$ m (trough, Figures 10a, 10c, 10e, 10g, and 10l, reference case simulation) and $A = 1$ m (bump, Figures 10b, 10d, 10f, 10h, and 10j). For the two configurations, and also for all the other simulations in this paper, wave-driven circulations and sediment transport are strong on the sandbar where waves break and are negligible in the vicinity of the offshore perturbation.

[46] For the initial situation with an offshore trough (reference case simulation, Figures 10a, 10c, 10e, 10g, and 10i corresponding to temporal evolution of Z_b in Figures 2b and 5a), wave refraction across the trough results in two wave energy focusing locations updrift and downdrift of the bathymetric anomaly at $x \approx -100$ m and 100 m, respectively (Figure 10a). The increasing wave heights at these locations lead to a larger amplitude of setup and set down in the surf and shoaling zone, respectively (Figure 10c). Alongshore gradients in radiation stress (Figure 10a) and pressure (Figure 10c) show slight patterns shoreward of the perturbation, and the vectorial sum resulting in the residual forcing $\vec{F}_r = \vec{F}_w + \vec{F}_p$ shows striking counterrotating patterns (Figure 10e) that characterizes the net forcing available to drive nearshore currents. In Figure 10e the wave-induced vorticity forcing term $F_v = \left(\vec{\nabla} \wedge (D\vec{e}_k)\right) \cdot \vec{e}_z$, which is superimposed, is essentially similar in pattern to $\vec{F}r$ (notice no circulation model has been run). This shows that rip current circulations are essentially driven by differential broken wave energy dissipation, i.e., without having to consider pressure gradients. The wave-driven circulations $\vec{U}$ and vorticity $\Gamma = \left(\vec{\nabla} \wedge \vec{U}\right) \cdot \vec{e}_z$ are shown in Figure 10g.

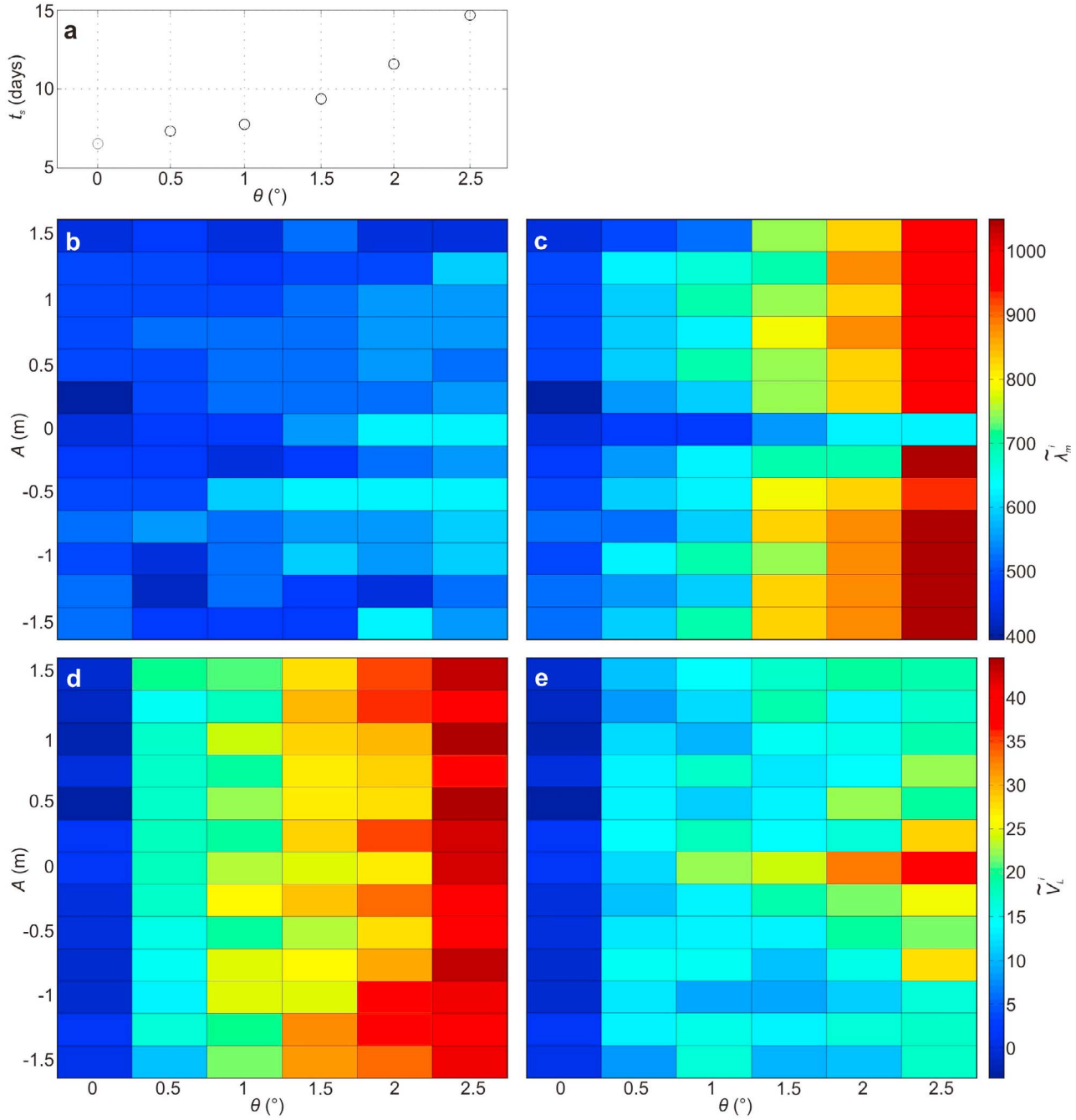

Figure 8. Mean rip spacing and rip channel alongshore migration at saturation time t_s as a function of the offshore perturbation height A and offshore wave angle to the shore θ for $d_b = 350$ m. (a) Saturation time t_s as a function of θ, (b) mean updrift rip spacing $\widetilde{\lambda}_m^u$, (c) mean downdrift rip spacing $\widetilde{\lambda}_m^d$, (d) updrift rip channel migration rate $\widetilde{V}_L^u$ and (e) downdrift rip channel migration rate $\widetilde{V}_L^d$.

A downdrift-skewed rip current is observed at $x \approx 0$ with a slightly undulating longshore current immediately to the right and to the left of the rip current.

[47] The resulting sediment transport fluxes $\vec{Q}_s$ and erosion/accretion patterns are shown in Figure 10i. An erosion area is observed shoreward of the offshore perturbation at $x \approx 0$, with the temporal evolution of the morphology eventually leading to the presence of the forced rip channel at $x \approx 0$ (Figure 6d). Two other erosion areas, yet less intense, are found at $x \approx -300$ m (updrift) and 400 m (downdrift) with the updrift erosion about 3 times larger than the downdrift one.

[48] The same analysis was done for the case of an offshore bump (Figures 10b, 10d, 10f, 10h, and 10j). For this situation wave refraction across the bump results in one localized wave energy focusing location shoreward of the bathymetric anomaly at $x \approx 0$ (Figure 10b). These forcing patterns have an opposite rotational nature with respect to the offshore trough situation (Figure 10e). This results in an onshore flow shoreward of the offshore bump at $x = 0$ and a

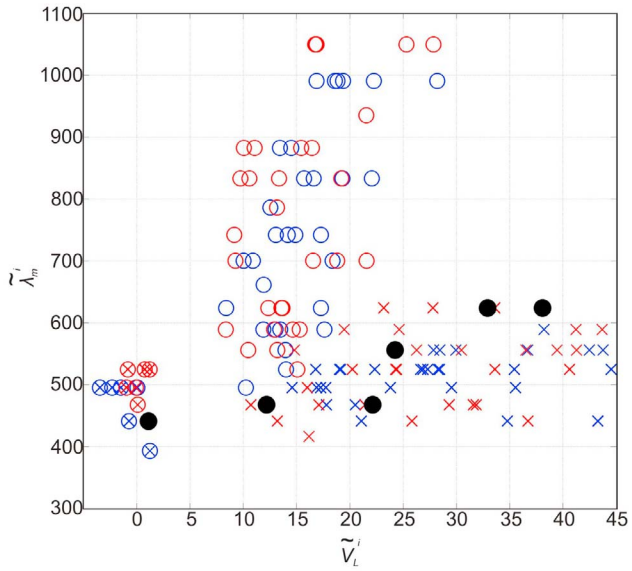

Figure 9. Mean rip spacing versus rip channel migration rate at saturation time t_s for d_b = 350 m: updrift (crosses), downdrift (circles) and alongshore-uniform scenario (thick circles). Red and blue correspond to simulations with an offshore trough and bump, respectively.

rip current immediately updrift at $x \approx -100$ m (Figure 10h). These circulations drive an accretion area shoreward of the offshore bump and two erosion areas to the right and to the left (Figure 10j).

[49] For smaller perturbation amplitude $|A|$ and/or larger wave angle θ, wave-induced vorticity forcing terms are similar in patterns but are less intense (not shown). Therefore, the degree of enforcement of the rip current circulation shoreward of the offshore perturbation decreases. As a result, rip channels can migrate past the $x = 0$ location (e.g., Figures 6g, 6h, 6j, 6k and 6l). For large perturbation amplitude $|A|$ and/or smaller wave angle θ, the degree of enforcement of the rip current circulation shoreward of the offshore bathymetric anomaly is large and the forced rip channel remains at the same alongshore location throughout the simulation.

[50] Figure 11 shows the same hydrodynamic analysis for the three situations addressing the influence of the offshore perturbation distance to the shore d_b in Figure 5. Wave refraction is similar in patterns for d_b = 350 m, 450 and 550 m, with two localized wave energy focusing locations updrift at $x \approx -100$ m and downdrift at $x \approx 100$ m (Figures 11a–11c). These wave focusing patterns are less intense and more diffused alongshore with increasing d_b (Figure 11). Accordingly, both the residual forcing $\vec{F}_r$ and wave-induced vorticity forcing term F_v show a rotational nature of similar pattern with less strength. Accordingly, there is less intense net rotational forcing available to drive nearshore currents with increasing d_b (Figures 11d–11f). Accordingly, nearshore currents are characterized by an undulating longshore current and a downdrift-skewed rip current (Figures 11g and 11h). The intensity of the enforced rip current decreases with increasing d_b. The refraction-induced intensification of net rotational forcing for a more shoreward positioned offshore perturbation explains why, for a given amplitude $|A|$, the influence of an offshore perturbation on surf zone rip channel evolution decreases with increasing perturbation distance to the shore d_b.

4.1.2. Temporal Evolution of Rip Channel Morphology and Wave-Driven Circulations

[51] The larger rip spacing downdrift of the offshore bathymetric anomaly cannot be explained through the examination of the wave-driven circulations and resulting sediment transport patterns at $t = 0$ alone as the presence of an offshore perturbation does not impact wave-driven circulations and resulting sediment transport patterns for $|x| >$ 500 m. Figure 12 shows in detail the evolution of the rip channels and wave-driven circulations for the reference case simulation ($A = -1$ m, $d_b = 350$ m, $H_s = 1.2$ m, $T_p = 10$ s and $\theta = 1°$), from $t = 0$ (Figure 12a) to saturation ($t = 7$ days in Figure 12h). At $t = 0$ (Figure 12a) a weak (≈ 0.2 m s^{-1}) skewed rip current shoreward of the offshore trough is driven by alongshore differential broken wave energy dissipation enforced by wave refraction (Figures 10a, 10c, 10e, 10g, and 10i). This rip current drives the rapid formation of a rip channel shoreward of the offshore perturbation at $t =$ 1 day (Figure 12b). Updrift of the perturbation, the circulation cell to the left of this rip channel is associated with an onshore flow across a rapidly developing shoal at $x \approx -100$ m (Figure 12b). The resulting clockwise circulation to the left of the shoal encounters the rightward longshore currents driven by wave obliquity along the alongshore-uniform section of the beach ($x < -500$ m), enforcing a rip current and the consecutive formation of a rip channel at $x \approx -400$ m (Figure 12b). This process explains the subsequent rapid formation of rip channels updrift (Figures 12b–12f), before free rip channels start to form at $t \approx 6$ days (Figures 12g and 12h).

[52] In contrast, downdrift of the perturbation the anticlockwise circulation cell to the right of the shoal (at $x \approx$ 100 m) is advected by the rightward longshore current (Figure 12b) resulting in a larger alongshore scale of the circulation cell. Downdrift of the perturbation, a rip channel therefore forms less rapidly and farther from the forced rip channel (at $x \approx 700$ m in Figure 12c) than updrift of the perturbation. This seems to drive an increase in the alongshore extent of the circulation associated with the first downdrift rip current. This effect cascades to the following 3–4 downdrift rip channels until it becomes negligible at about the end of the downdrift domain and the spacing goes back to the value associated with the simulations starting with an alongshore-uniform bathymetry. Accordingly, although downdrift rip channels are exposed to an alongshore-uniform wavefield similar to that of the rest of the domain (as the influence of the offshore bathymetric anomaly on hydrodynamics is significant only at about $x < 500$ m) downdrift rip channels self-organize into patterns with different length scales and migration rates than the free rip channels.

4.2. Qualitative Comparison With Observations

[53] Contrasting updrift/downdrift rip channel behavior for an idealized configuration as the one of this study is obviously difficult to find in the field. This requires an accurate high-frequency monitoring of the sandbar geometry with concurrent wave data acquisition at a site exhibiting a

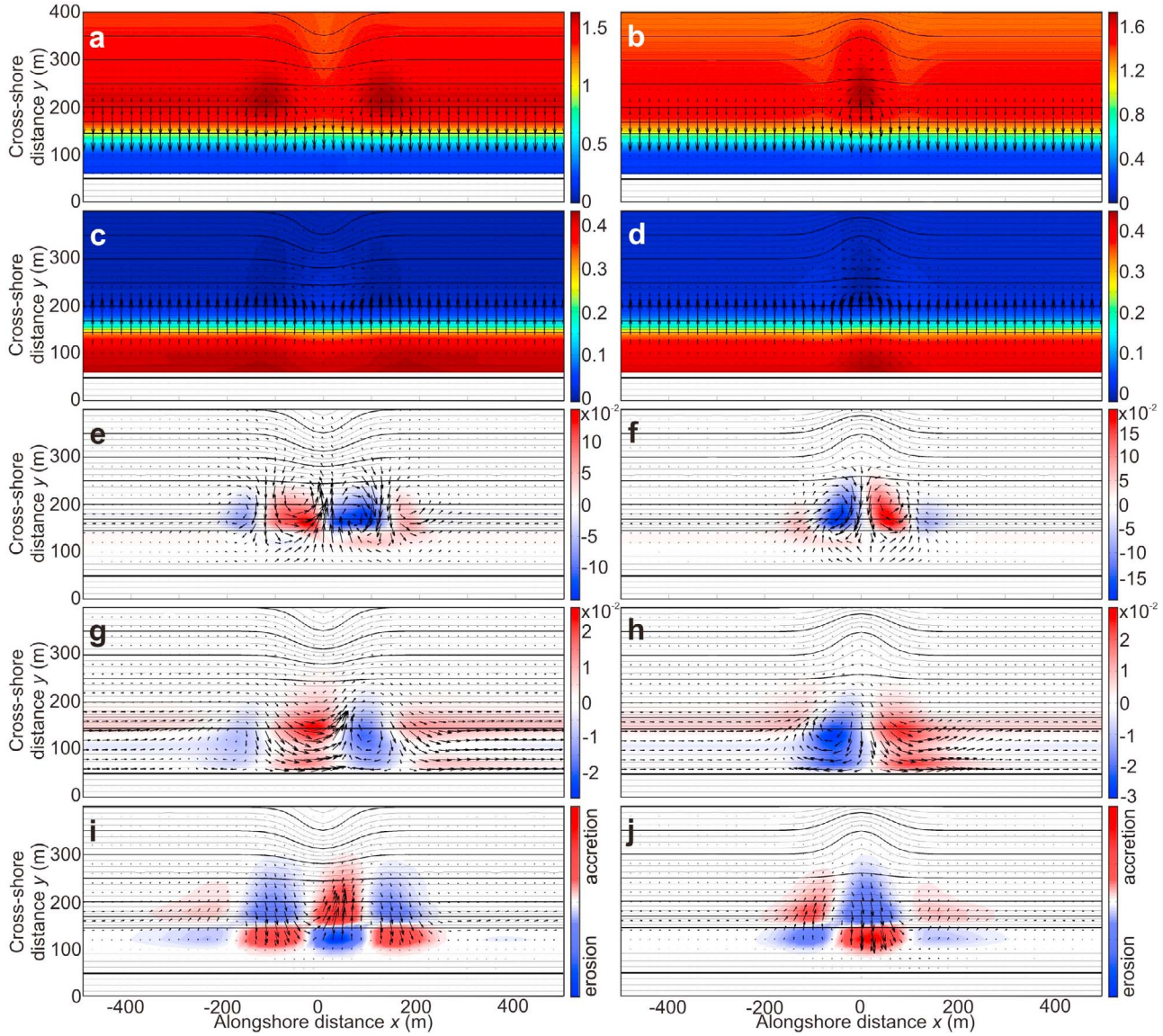

Figure 10. Hydrodynamics and sediment transport patterns at $t = 0$ for offshore waves with $H_s = 1.2$ m, $T_p = 10$ s and $\theta = 1°$ and for two alongshore nonuniform situations with an offshore perturbation at $x = 0$ and $d_b = 350$ m with (left) $A = -1$ m (reference case simulation) and (right) $A = 1$ m (bump). (a, b) Wave-field with color bar indicating significant wave height H_s in meters and resulting gradients in radiation stress $\vec{F}_w$ (arrows). (c, d) Pressure gradients F_p (m^2 s^{-2}) (arrows) superimposed on the η field with color bar indicating η in meters. (e, f) Residual forcing $\vec{F}_r = \vec{F}_p + \vec{F}_w$ (arrows) superimposed on the vorticity forcing term field related to differential broken wave energy dissipation $F_v = \left(\vec{\nabla} \wedge (D\vec{e}_k)\right) \cdot \vec{e}_z$ (kg m^{-2} s^{-2}). (g, h) Resulting wave-driven circulations $\vec{U}$ (arrows) and vorticity $\Gamma = \left(\vec{\nabla} \wedge \vec{U}\right) \cdot \vec{e}_z$ (s^{-1}) and (i, j) sediment transport fluxes $\vec{Q}_s$ (arrows) with erosion (blue) and accretion (red) patterns. Isobaths (0.5 m intervals) are contoured in the background.

single, persistent, offshore perturbation. A wave-dominated beach site meeting these criteria is Duck, North Carolina, extensively described by *Lippmann and Holman* [1990] and monitored with an ARGUS video system [*Holman and Stanley*, 2007]. Figure 13 shows a typical sandbar downstate sequence starting from an alongshore-uniform sandbar geometry (Figure 13a) progressively evolving toward a typical bar and rip morphology (Figure 13k). At Duck, a persistent offshore trough, formed by scouring by the Field Research Facility bridge piers [e.g., *Lee and Birkemeier*, 1993] is located at $x \approx 0$ in Figure 13 with a maximum amplitude of about 1–1.5 m. During the downstate sequence in Figure 13 crescentic patterns develop and subsequently attach to the beach with a rip spacing larger downdrift of the pier ($\lambda \approx 500$ m at $x < 0$ with respect to prevailing wave conditions, see the downdrift bar and rip orientation in Figures 13g–13k) than updrift of the pier ($\lambda \approx 350$–400 m at $x > 0$). This contrasting rip spacing is also readily apparent in

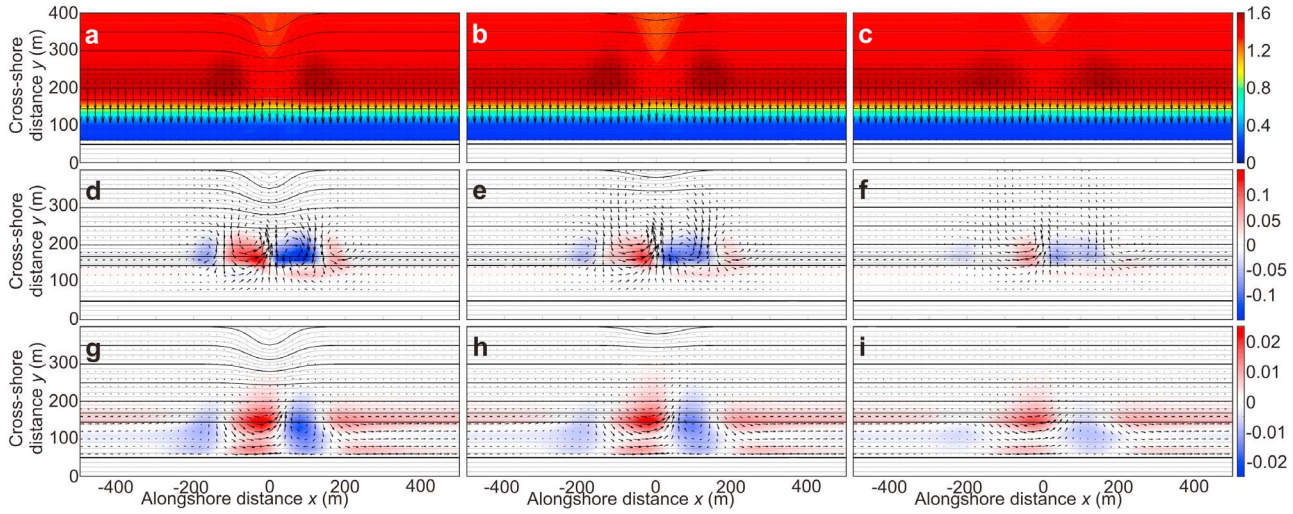

Figure 11. Hydrodynamics at $t = 0$ for offshore waves with $H_s = 1.2$ m, $T_p = 10$ s and $\theta = 1.5°$ and corresponding to the situations given in Figure 5 with an offshore trough ($A = -1$ m) at $x = 0$ and with a distance to the shore (left) $d_b = 350$ m (reference case simulation), (middle) $d_b = 450$ m and (right) $d_b = 550$ m. (a, b, c) Wavefield with color bar indicating significant wave height H_s in meters and resulting gradients in radiation stress $\vec{F}_w$ (arrows). (d, e, f) Residual forcing $\vec{F}_r = \vec{F}_p + \vec{F}_w$ (arrows) superimposed on the vorticity forcing term field related to differential broken wave energy dissipation $F_v = \left(c\vec{\nabla} \wedge (D\vec{e}_k)\right) \cdot \vec{e}_z$ (kg m^{-2} s^{-2}). (g, h, i) Resulting wave-driven circulations $\vec{U}$ (arrows) and vorticity $\Gamma = \left(\vec{\nabla} \wedge \vec{U}\right) \cdot \vec{e}_z$ (s^{-1}). Isobaths (0.5 m intervals) are contoured in the background.

a planview image at Duck of *Plant et al.* [2006]. This 11 day event at Duck 1998 following Hurricane Bonnie at $t \approx$ 237 days is part of a longer sequence that has been extensively studied for other purposes [e.g., *Van Enckevort et al.*, 2004; *Plant et al.*, 2006; *Tiessen et al.*, 2010].

[54] This observation supports qualitatively our numerical results. We cannot rule out that additional processes contribute to the contrasting sandbar behavior updrift and downdrift of the pier. For instance, the mean cross-shore sandbar position at the beginning of the down-state sequence could have been slightly different updrift and downdrift. As rip spacing is highly sensitive to the beach profile prior to pattern development, with typically rip spacing increasing with increasing sandbar distance to the shore [*Calvete et al.*, 2007], alongshore difference in beach profile at the peak of the storm could also explain the contrasting rip spacings observed updrift and downdrift of the offshore trough. Another potential explanation is the presence of preexisting, yet slightly developed, sandbar alongshore rhythmicity at the peak of the storm with different length scales updrift and downdrift. These preexisting patterns can impact the subsequent development of the rip channels [*Tiessen et al.*, 2011].

4.3. Model Limitations

[55] There are a number of model limitations in our study. To simplify, as indicated in section 2.1.2, we neglected the wave group scale forcing (narrow banded swells are used throughout this study) and the 3-D structure of nearshore circulations. As we addressed reasonably low amplitude offshore perturbation ($|A| \leq 1.5$ m), we also neglected wave scattering and reflection that can be significant for the case of an offshore perturbation with abrupt bathymetric changes [e.g., *Bender and Dean*, 2003]. We did not address the impact of the alongshore width of the offshore perturbation on surf zone rip channels. Additional simulations (not shown here) show that increasing the width of the bathymetric anomaly results in wave focusing patterns that are more diffuse alongshore. The less intense and more spread alongshore net rotational forcing available to drive nearshore currents decreases the influence of the offshore perturbation on surf zone rip channel evolution. The impact of the offshore perturbation on rip channels increases with decreasing perturbation width up to a point when wave scattering and reflection becomes significant which is out of bound of the validity of our numerical model. Furthermore, we did not address the effect of multiple offshore anomalies on nearshore rip evolution.

[56] For $\theta \geq 3.5°$ our numerical results are distorted by the lateral boundary conditions as downdrift rip channels rapidly enter the updrift domain before free rip channels have the time to develop. A small number of additional simulations with a longer domain showed that, for $\theta \geq 3°$, the distance from the offshore perturbation at which downdrift rip channels form increases with increasing θ and that the general behavior described in this paper for $\theta < 3°$ is not affected by the alongshore length of the domain.

[57] The typical growth time of 3-D surf zone patterns (here the free rip channels) increases with decreasing initial bed perturbation amplitude and increasing θ [e.g., *Garnier et al.*, 2008]. In our approach the initial random perturbations in the seabed are of the order of 1 mm, which is very small in comparison to the vertical amplitude of preexisting morphology (e.g., ripples) at the beginning of the down-state sequence. As bed form growth time decreases with increasing magnitude of the random perturbations, this explains the large typical growth times computed herein. This also

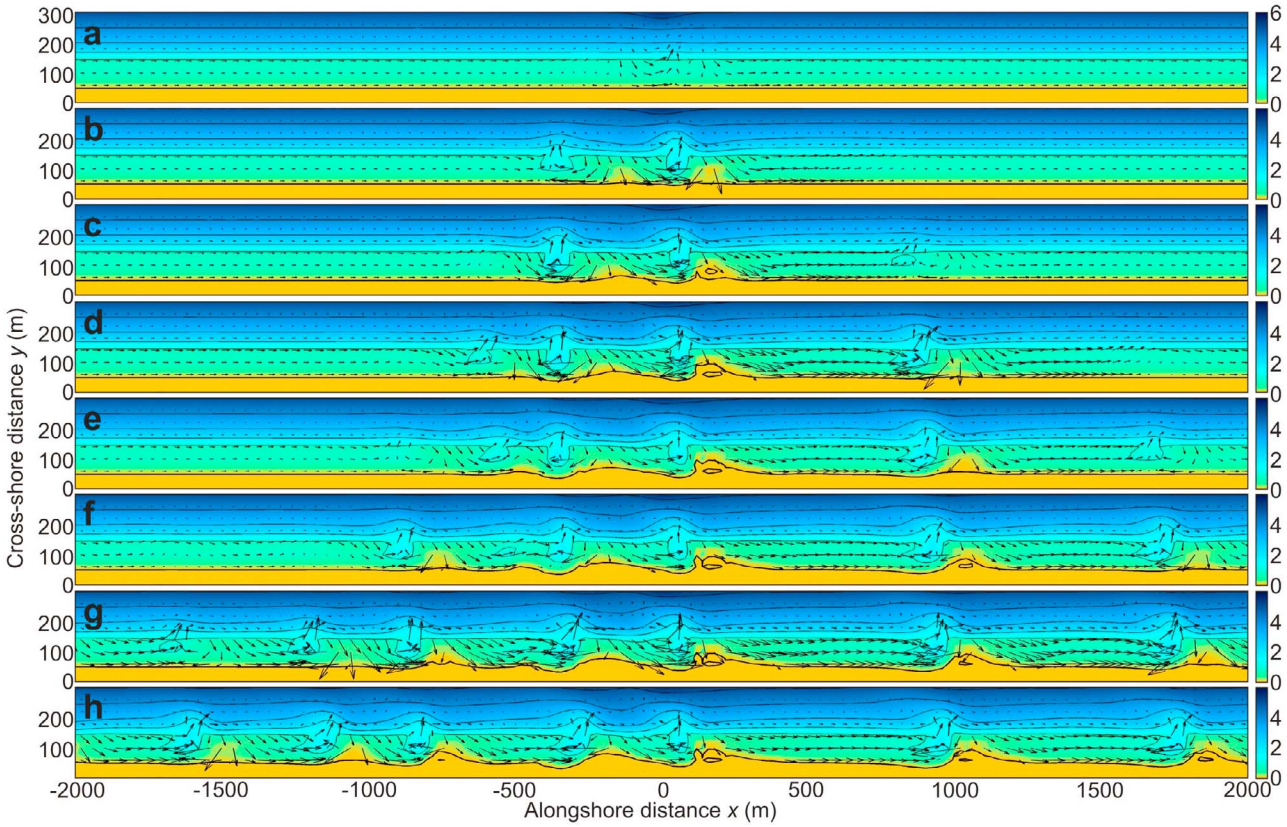

Figure 12. Zoom of the bathymetry at -2000 m $< x <$ 2000 m and $0 < y <$ 300 m with superimposed wave-induced currents (arrows, one out of two vectors are plotted in both directions) for offshore waves with H_s = 1.2 m, T_p = 10 s and θ = 1.5° starting from the alongshore nonuniform beach with an offshore perturbation at x = 0 with $A = -$ 1 m (trough) and d_b = 350 m (reference case simulation) at (a) t = 0, (b) t = 1 day, (c) t = 2 days, (d) t = 3 days, (e) t = 4 days, (f) t = 5 days, (g) t = 6 days and (h) t = 7 days when saturation is reached. Color bars indicate seabed elevation in meters, and isobaths (1 m intervals) are contoured in the background.

explains why, for the 1 mm amplitude initial random perturbations implemented in the model, rip channels do not form for $\theta >$ 6–7°,whereas field observations suggest that 3-D patterns are progressively damped for about $\theta >$ 30° [*Price and Ruessink*, 2011].

4.4. Proof of Concept and Implications

[58] Despite being exposed to the same wave conditions, downdrift and updrift rip channels self-organize into features with different alongshore scales and migration rates. A similar observation was made by *Tiessen et al.* [2011], who used a nonlinear morphodynamic model to address the influence of preexisting, small-amplitude, rhythmic surf zone bed forms on the subsequent evolution of rip channels. They concluded that, for a given offshore wave forcing, rip channels can self-organize into a range of different alongshore scales depending on the initial bathymetry. *Reniers et al.* [2004] used an alongshore nonuniform wavefield by including directional spreading in the initial wave conditions. They showed that the directional spreading affects the behavior of rip channels, with rip spacing depending on the directional spreading. These results appear to apply also to our study as different alongshore scales and migration rates are excited by the offshore bathymetric anomaly feeding back onto wave forcing through wave refraction.

[59] Overall, our work demonstrates that the behavior of an individual element of the surf zone system, herein rip channels, contrasts with the behavior of the wider nearshore system, suggesting that the approach of studying each nearshore element in isolation can limit our understanding of field observations. It therefore corroborates recent field evidence of interactions between shoreline evolution and offshore geological framework and stimulates further numerical and field studies addressing the nearshore system as a whole, that is, encompassing shoreline undulation (and erosional hot spots), sandbar(s) and offshore slowly evolving features.

5. Conclusion

[60] Using a nonlinear morphodynamic model we showed that the presence of a single offshore bathymetric anomaly strongly affects the formation, subsequent nonlinear evolution and saturation of surf zone rip channels. Despite the enforced wave-driven circulation patterns being highly different for an offshore bump and an offshore trough, a forced rip channel shoreward of the offshore bathymetric anomaly systematically forms under oblique wave incidence. The rip

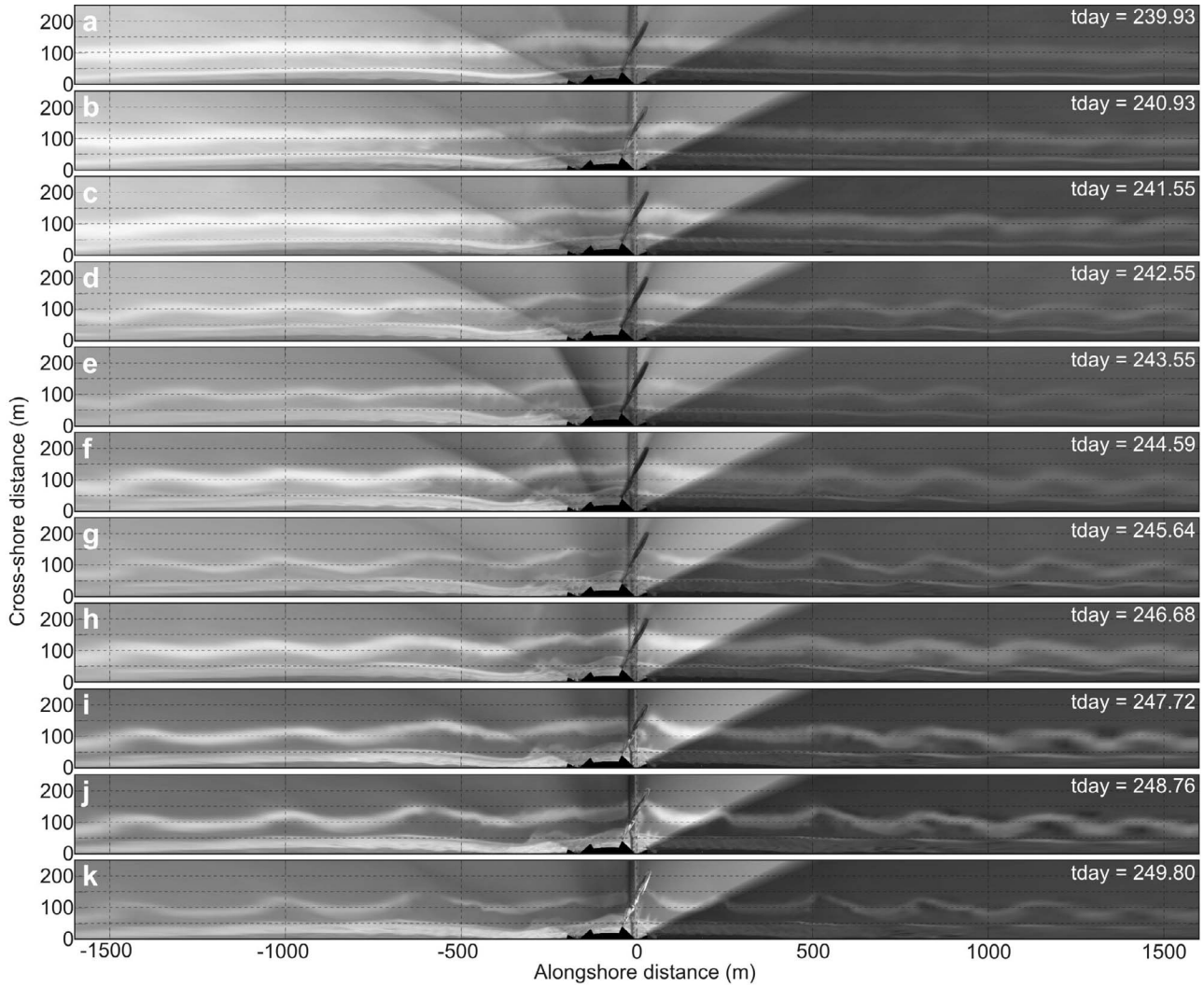

Figure 13. Sequence of rectified time exposure images at Duck Beach from 28 August (tday = 239) to 7 September (tday = 249) 1998 with the rip channels indicated by dark cuts through the white nearshore dissipation patterns across the sandbar. Duck exhibits a persistent offshore trough at the pier ($x \approx 0$). From top to bottom, sandbar evolution is characterized by a typical down-state sequence (3-D patterns develop from an alongshore-uniform sandbar geometry) with smaller rip spacing updrift ($x > 0$) than downdrift ($x < 0$) with respect to the prevailing wave conditions during this event that supports our numerical exercise.

channel can subsequently migrate downdrift or remain at the same alongshore location throughout the simulation. The stability in the location of this forced rip channel increases with increasing perturbation amplitude $|A|$, decreasing offshore wave obliquity, and decreasing perturbation distance to the shore. When the offshore perturbation amplitude $|A|$ is large and wave obliquity θ is small, updrift rip channels continuously merge to the forced rip channel and updrift rip channels cannot enter the downdrift domain. Rip channel behavior is essentially controlled by the strength of surf zone rip current circulations enforced by wave refraction across the offshore bathymetric anomaly. We additionally showed that the strength of initial surf zone rip current circulations is governed by differential broken wave energy dissipation (equation (17)), without having to consider alongshore pressure gradients, as traditionally done in the literature.

[61] Simulations show that, in the range of wave and bathymetric conditions addressed in this study, rip channel behavior downdrift and updrift of the preexisting offshore bathymetric anomaly is highly contrasting. Downdrift rip channels have systematically larger alongshore scales, smaller alongshore migration rates and more erosive megacusps than those updrift. Therefore, for a given offshore wave forcing, rip channels can self-organize into features of different alongshore scales and migration rates. This contrasting behavior can be excited by the presence of preexisting, small-amplitude, rhythmic surf zone bed forms [*Tiessen et al.*, 2011], an alongshore nonuniform wavefield by including directional spreading in the initial wave conditions [*Reniers et al.*, 2004] or an alongshore perturbation in the wavefield enforced by wave refraction across an offshore bathymetric anomaly (present study). Despite being highly idealized, our simulations are qualitatively

corroborated by video observations of sandbar behavior during a down-state sequence for shore-oblique waves at a site with a persistent offshore trough.

[62] **Acknowledgments.** This work was done within the framework of the project BARBEC (ANR 2010 JCJC 602 01). B.G.R. acknowledges additional funding by the Netherlands Organisation for Scientific Research (NWO) under contract 818.01.009. G.C. funded by the Cantabria Campus International (Augusto Gonzales Linares Program) and NIWA. N.B. funded by a postdoctoral research grant from the Fundacao para a Ciencia (SFRH/BPD/67041/2009). The wavelet computations in this paper were based on software developed by Aslak Grinsted and coworkers (version wtc-r14, available from http://www.pol.ac.uk/home/research/waveletcoherence/). We thank Timothy Price for his corrections and acknowledge the two anonymous reviewers, the Associate Editor and the Editor for their insightful comments.

References

Almar, R., B. Castelle, B. G. Ruessink, N. Sénéchal, P. Bonneton, and V. Marieu (2010), Two- and three-dimensional double-sandbar system behaviour under intense wave forcing and a meso-macro tidal range, *Cont. Shelf Res.*, *30*, 781–792.

Austin, M., T. M. Scott, J. W. Brown, J. A. Brown, J. H. MacMahan, G. Masselink, and P. Russell (2010), Temporal observations of rip current circulation on a macro-tidal beach, *Cont. Shelf Res.*, *30*, 1149–1165.

Bailard, J. A. (1981), An energetics total load sediment transport model for a plane beach, *J. Geophys. Res.*, *86*(C11), 10,938–10,954.

Battjes, J. A. (1975), Modeling of turbulence in the surf zone, paper presented at Symposium on Modeling Techniques, Am. Soc. of Civ. Eng., San Francisco, Calif.

Battjes, J. A., and J. Janssen (1978), Energy loss and set-up due to breaking in random waves, paper presented at 16th International Conference on Coastal Engineering, Am. Soc. of Civ. Eng., New York.

Battjes, J. A., and M. J. F. Stive (1985), Calibration and verification of a dissipation model for random breaking waves, *J. Geophys. Res.*, *90*(C5), 9159–9167.

Bender, C. J., and R. G. Dean (2003), Wave field modification by bathymetric anomalies and resulting shoreline changes: A review with recent results, *Coastal Eng.*, *49*, 125–153.

Bender, C. J., and R. G. Dean (2005), Wave transformation by axisymmetric three-dimensional bathymetric anomalies with gradual transitions in depth, *Coastal Eng.*, *52*, 331–351.

Bonneton, P., N. Bruneau, B. Castelle, and F. Marche (2010), Large-scale vorticity generation due to dissipating waves in the surf zone, *Discrete Contin. Dyn. Syst., Ser. B*, *13*(4), 729–738.

Booij, N., R. C. Ris, and L. H. Holthuijsen (1999), A third-generation wave model for coastal regions: 1. Model description and validation, *J. Geophys. Res.*, *104*(C4), 7649–7666.

Brander, R. W., and P. J. Cowell (2003), A trend-surface technique for discrimination of surf-zone morphology: Rip current channels, *Earth Surf. Processes Landforms*, *28*, 905–918.

Brander, R. W., and A. D. Short (2000), Morphodynamics of a large-scale rip current system at Muriwai Beach, New Zealand, *Mar. Geol.*, *165*, 27–39.

Browder, A. G., and J. E. McNinch (2006), Linking framework geology and nearshore morphology: Correlation of paleo-channels with shore-oblique sandbars and gravel outcrops, *Mar. Geol.*, *231*, 141–162.

Bruneau, N., B. Castelle, P. Bonneton, R. Pedreros, R. Almar, N. Bonneton, P. Bretel, J. P. Parisot, and N. Sénéchal (2009), Field observations of an evolving rip current on a meso-macrotidal well-developed inner bar and rip morphology, *Cont. Shelf Res.*, *29*, 1650–1662.

Bruneau, N., P. Bonneton, B. Castelle, and R. Pedreros (2011), Modeling rip current circulations and vorticity in a high-energy mesotidal-macrotidal environment, *J. Geophys. Res.*, *116*, C07026, doi:10.1029/2010JC006693.

Calvete, D., N. Dodd, A. Falqués, and S. M. van Leeuwen (2005), Morphological development of rip channel systems: Normal and near-normal wave incidence, *J. Geophys. Res.*, *110*, C10006, doi:10.1029/2004JC002803.

Calvete, D., G. Coco, A. Falqués, and N. Dodd (2007), (Un)predictability in rip channel systems, *Geophys. Res. Lett.*, *34*, L05605, doi:10.1029/2006GL028162.

Castelle, B., and P. Bonneton (2006), Modelling of a rip current induced by waves over a ridge and runnel system on the Aquitanian Coast, France, *C. R. Geosci.*, *338*, 711–717.

Castelle, B., and B. G. Ruessink (2011), Modeling formation and subsequent nonlinear evolution of rip channels: Time-varying versus time-invariant wave forcing, *J. Geophys. Res.*, *116*, F04008, doi:10.1029/2011JF001997.

Castelle, B., B. G. Ruessink, P. Bonneton, V. Marieu, N. Bruneau, and T. D. Price (2010a), Coupling mechanisms in double sandbar systems, Part 1: Patterns and physical explanation, *Earth Surf. Processes Landforms*, *35*, 476–486.

Castelle, B., B. G. Ruessink, P. Bonneton, V. Marieu, N. Bruneau, and T. D. Price (2010b), Coupling mechanisms in double sandbar systems, Part 2: impact on alongshore variability of inner-bar rip channels, *Earth Surf. Processes Landforms*, *35*, 771–781.

Castelle, B., H. Michallet, V. Marieu, F. Leckler, B. Dubardier, A. Lambert, C. Berni, P. Bonneton, E. Barthélemy, and F. Bouchette (2010c), Laboratory experiment on rip current circulations over a moveable bed: Drifter measurements, *J. Geophys. Res.*, *115*, C12008, doi:10.1029/2010JC006343.

Coco, G., and A. B. Murray (2007), Patterns in the sand: from forcing templates to self-organization, *Geomorphology*, *91*, 271–290.

Dalrymple, R. A., J. H. MacMahan, A. J. H. M. Reniers, and V. Nelko (2011), Rip currents, *Annu. Rev. Fluid Mech.*, *43*, 551–581.

Deigaard, R., N. Drønen, J. Fredsøe, J. H. Jensen, and M. P. Jørgensen (1999), A morphological stability analysis for a long straight barred coast, *Coastal Eng.*, *36*, 171–195.

Drønen, N., and R. Deigaard (2007), Quasi-three-dimensional modelling of the morphology of longshore bars, *Coastal Eng.*, *54*, 197–215.

Falqués, A., A. Montoto, and V. Iranzo (1996), Bed-flow instability of the longshore current, *Cont. Shelf Res.*, *16*, 1927–1964.

Falqués, A., G. Coco, and D. A. Huntley (2000), A mechanism for the generation of wave-driven rhythmic patterns in the surf zone, *J. Geophys. Res.*, *105*, 24,071–24,088.

Falqués, A., N. Dodd, R. Garnier, F. Ribas, L. C. MacHardy, P. Larroudé, D. Calvete, and F. Sancho (2008), Rhythmic surf zone bars and morphodynamic self-organization, *Coastal Eng.*, *55*, 622–641.

Falqués, A., D. Calvete, and F. Ribas (2011), Shoreline instability due to very oblique wave incidence: Some remarks on the physics, *J. Coastal Res.*, *27*, 291–295.

Garnier, R., D. Calvete, A. Falqués, and M. Caballeria (2006), Generation and nonlinear evolution of shore-oblique/transverse sand bars, *J. Fluid Mech.*, *567*, 327–360.

Garnier, R., D. Calvete, A. Falqués, and N. Dodd (2008), Modelling the formation and the long-term behavior of rip channel systems from the deformation of a longshore bar, *J. Geophys. Res.*, *113*, C07053, doi:10.1029/2007JC004632.

Garnier, R., N. Dodd, A. Falqués, and D. Calvete (2010), Mechanisms controlling crescentic bar amplitude, *J. Geophys. Res.*, *115*, F02007, doi:10.1029/2009JF001407.

Grinsted, A., J. C. Moore, and S. Jevrejeva (2004), Application of the cross wavelet transform and wavelet coherence to geophysical time series, *Nonlinear Processes Geophys.*, *11*, 561–566.

Haas, K. A., and I. A. Svendsen (2002), Laboratory measurements of the vertical structure of rip currents, *J. Geophys. Res.*, *107*(C5), 3047, doi:10.1029/2001JC000911.

Holman, R. A., and J. Stanley (2007), The history and technical capabilities of argus, *Coastal Eng.*, *54*, 477–491.

Idier, D., A. Falqués, B. G. Ruessink, and R. Garnier (2011), Shoreline instability under low-angle wave incidence, *J. Geophys. Res.*, *116*, F04031, doi:10.1029/2010JF001894.

Jevrejeva, S., J. C. Moore, and A. Grinsted (2003), Influence of the Arctic Oscillation and El Niño–Southern Oscillation (ENSO) on ice conditions in the Baltic Sea: The wavelet approach, *J. Geophys. Res.*, *108*(D21), 4677, doi:10.1029/2003JD003417.

Klein, M. D., and H. M. Schuttelaars (2006), Morphodynamic evolution of double-barred beaches, *J. Geophys. Res.*, *111*, C06017, doi:10.1029/2005JC003155.

Lee, G., and W. A. Birkemeier (1993), Beach and nearshore survey data: 1985–1991 CERC Field Research Laboratory, *Tech. Rep. CERC-93-3*, U.S. Army Corps of Eng., Waterways Exp. Stn., Vicksburg, Miss.

Lippmann, T., and R. Holman (1990), The spatial and temporal variability of sand bar, *J. Geophys. Res.*, *95*(C7), 11,575–11,590.

Long, J. W., and H. T. Özkan-Haller (2005), Offshore controls on nearshore rip currents, *J. Geophys. Res.*, *110*, C12007, doi:10.1029/2005JC003018.

Longuett-Higgins, M. S., and R. W. Stewart (1964), Radiation stress in water waves, a physical discussion with applications, *Deep Sea Res.*, *11*(4), 529–563.

MacMahan, J. H., E. B. Thornton, and A. J. H. M. Reniers (2006), Rip current review, *Coastal Eng.*, *53*, 191–208.

McNinch, J. E. (2004), Geologic control in the nearshore: shore-oblique sandbars and shoreline erosion hotspots, Mid-Atlantic Bight, USA, *Mar. Geol.*, *211*, 121–141.

Mei, C. C. (1989), *Applied Dynamics of Ocean Waves*, World Sci., Singapore.

Orzech, M. D., A. J. H. M. Reniers, E. B. Thornton, and J. H. MacMahan (2011), Megacusps on rip channel bathymetry: Observations and modeling, *Coastal Eng.*, *58*, 890–907.

Phillips, O. M. (1977), *The Dynamics of the Upper Ocean*, Cambridge Univ. Press, Cambridge, U. K.

Plant, N. G., K. T. Holland, and R. A. Holman (2006), A dynamical attractor governs beach response to storms, *Geophys. Res. Lett.*, *33*, L17607, doi:10.1029/2006GL027105.

Price, T. D., and B. G. Ruessink (2011), State dynamics of a double sandbar system, *Cont. Shelf Res.*, *31*, 659–674.

Reniers, A. J. H. M., J. A. Roelvink, and E. B. Thornton (2004), Morphodynamic modeling of an embayed beach under wave group forcing, *J. Geophys. Res.*, *109*, C01030, doi:10.1029/2002JC001586.

Ris, R. C., L. H. Holthuijsen, and N. Booij (1999), A third-generation wave model for coastal regions: 2. Verification, *J. Geophys. Res.*, *104*(C4), 7667–7681.

Ruessink, B. G., G. Coco, R. Ranasinghe, and I. L. Turner (2007), Coupled and noncoupled behavior of three-dimensional morphological patterns in a double sandbar system, *J. Geophys. Res.*, *112*, C07002, doi:10.1029/2006JC003799.

Schielen, R., A. Doelman, and H. E. De Swart (1993), On the dynamics of free bars in straight channels, *J. Fluid Mech.*, *252*, 325–356.

Schupp, C. A., J. E. McNinch, and J. H. List (2006), Nearshore shore-oblique bars, gravel outcrops, and their correlation to shoreline change, *Mar. Geol.*, *233*, 63–79.

Scott, T. M., P. Russell, G. Masselink, and A. Woolers (2009), Rip current variability and hazard along macro-tidal coast, *J. Coast. Res.*, *SI 56*, 895–898.

Shepard, F. P., and D. L. Inman (1950), Nearshore water circulation related to bottom topography and wave refraction, *Eos Trans. AGU*, *31*, 196–212.

Smit, M. W. J., A. J. H. M. Reniers, B. G. Ruessink, and J. A. Roelvink (2008), The morphological response of a nearshore double sandbar system to constant wave forcing, *Coastal Eng.*, *55*, 761–770.

Smith, J. (2006), Wave-current interactions in finite depth, *J. Phys. Oceanogr.*, *36*, 1403–1419.

Thornton, E. B., J. H. MacMahan, and A. H. Sallenger Jr. (2007), Rip currents, mega-cusps, and eroding dunes, *Mar. Geol.*, *240*, 151–167.

Tiessen, M. C. H., S. M. Van Leeuwen, D. Calvete, and N. Dodd (2010), Field test of a linear stability model for crescentic sandbar, *Coastal Eng.*, *57*, 41–51.

Tiessen, M. C. H., N. Dodd, and R. Garnier (2011), Development of crescentic bars for a periodically perturbed initial bathymetry, *J. Geophys. Res.*, *116*, F04016, doi:10.1029/2011JF002069.

Torrence, C., and G. P. Compo (1998), A practical guide to wavelet analysis, *Bull. Am. Meteorol. Soc.*, *79*, 61–78.

Van Enckevort, I. M. J., and B. G. Ruessink (2003), Video observations of nearshore bar bahaviour. Part 2: alongshore non-uniform variability, *Cont. Shelf Res.*, *23*, 513–532.

Van Enckevort, I. M. J., B. G. Ruessink, G. Coco, K. Susuki, I. L. Turner, N. G. Plant, and R. A. Holman (2004), Observations of nearshore crescentic sandbars, *J. Geophys. Res.*, *109*, C06028, doi:10.1029/2003JC002214.

Van Rijn, L. C. (1989), *Handbook of Sediment Transport by Currents and Waves*, Delft Hydraul., Delft, Netherlands.

Vis-Star, N., H. de Swart, and D. Calvete (2008), Patch behaviour and predictability properties of modelled finite-amplitude sand ridges on the inner shelf, *Nonlinear Processes Geophys.*, *15*, 943–955.

Wijnberg, K. M., and A. Kroon (2002), Barred beaches, *Geomorphology*, *48*, 103–120.

Wright, L. D., and A. D. Short (1984), Morphodynamic variability of surf zones and beaches: A synthesis, *Mar. Geol.*, *56*, 93–118.

P. Bonneton, B. Castelle, and V. Marieu, UMR EPOC 5805, Université de Bordeaux, CNRS, Avenue des Facultés, F-33405 Talence CEDEX, France. (b.castelle@epoc.u-bordeaux1.fr)

N. Bruneau, National Laboratory of Civil Engineering, Estuaries and Coastal Zones Division, Av. do Brasil, 101, P-1700-066 Lisbon, Portugal.

G. Coco, Environmental Hydraulic Institute, IH Cantabria, Universidad de Cantabria, c/Isabel Torres 15, E-39011 Santander, Spain.

B. G. Ruessink, Institute for Marine and Atmospheric Research, Department of Physical Geography, Faculty of Geosciences, Utrecht University, PO Box 80.115, NL-3508 TC Utrecht, Netherlands.